POLITECNICO DI MILANO
FACOLTÀ DI INGEGNERIA INDUSTRIALE E DELL'INFORMAZIONE
Corso di Laurea Magistrale in Ingegneria Fisica

Optical characterization of squared and parabolic SiGe QWs: absorption and photoreflectance

Supervisor: Dr. Daniel Chrastina
Assistant Supervisor: Ing. Jacopo Frigerio

Graduation thesis of:
Stefano Sem
Id number: 832886

Academic Year 2016 - 2017

Contents

1 SiGe heterostructures **11**
- 1.1 SiGe heterostructures in opto-electronic devices 11
- 1.2 Square QW 12
  - 1.2.1 QW samples 15
- 1.3 Parabolic QW 19
  - 1.3.1 PQW samples 20
- 1.4 Optical properties of Quantum Wells 22
  - 1.4.1 Inter-band and intra-band transition 22
  - 1.4.2 Absorption coefficient in 2D system 23
- 1.5 *Nextnano* Software 25

2 Sample growth and XRD analysis **27**
- 2.1 LEPECVD 27
- 2.2 XRD analysis 29
  - 2.2.1 Von Laue condition 29
  - 2.2.2 $\omega - 2\theta$ Scan in a QW structure 31
  - 2.2.3 'Xrayutilites' simulation 32
  - 2.2.4 XRD diffractometer 33

3 Absorption and photoreflectance measurements **36**
- 3.1 Absorption measurements 36
  - 3.1.1 Setup in absorption measurement 37
  - 3.1.2 Optical density and data acquisition 38
  - 3.1.3 QW/PQW absorption measurements 39
- 3.2 Modulation spectroscopy 42
  - 3.2.1 Setup in photoreflectance measurements 44
  - 3.2.2 Data acquisition and fitting 45
  - 3.2.3 Measurements 47

4 Results **49**
4.1 Square QW 49
4.2 Parabolic QW 53

List of Figures

1.1 Schematic view of a modulator, waveguide and detector system 11
1.2 First three bound states in a GaAs finite square quantum well of width $a = 10$ nm and depth $V_0 = 0.3$ eV 13
1.3 (a) Potential well with confined state placed at the right energy. (b) Total energy. (c) Density of state of a 2D system (steplike), and a 3D shape (parabolic) 15
1.4 Schematic representation of Type I (a) and Type II (b) band alignment. Quantum well made of Type I (c), and quantum well made of Type II (d). 16
1.5 (a) Fundamental bandgap energies (with respective **k** point); (b) VBO; (c) CBO; (d) band-edge profile for QWs structure with $Si_{1-x}Ge_x$ layer on a $Si_{1-y}Ge_y$ VS. 17
1.6 Structure of sample 10082. QW is repeated 50 times 18
1.7 Band-edges of c-gamma, light hole and heavy hole in the growth direction of sample 10082 (10nm well and 20 nm barrier). 19
1.8 $\psi(z)$ solutions of the equation 1.1 20
1.9 Conduction and valence band-edges at Γ point for (a)10230 nominal thickness and (b)10039 nominal thickness 21
1.10 Band-edge of the conduction band at the Γ point. Square modulus of confined solutions is shown. The barrier is $SiGe_{0.85}$ while the central point of the well is pure germanium, the calculations are made using Nextnano 22
1.11 Example of a JDOS for a 2D system (from reference [6]). . . . 24

2.1 Schematic representation of the LEPECVD deposition chamber 28
2.2 Ratio between thickness of deposited material and nominal . 29

2.3 Schematic representation of x-ray scattering in a lattice. Q, B, P are respectively the source, the detector and a generic scattering center. The vector **r** relate the origin of the system and the scattering point P. 31
2.4 $\omega - 2\vartheta$ scan of the (0 0 4) peak of sample 10082-F7, in red the measured intensity is shown, the green curve is due to the Ge wells while the blue one is due to the SiGe barriers. 33
2.5 XRD $\omega - 2\vartheta$ around the (0 0 4) diffraction peak of a PQW sample 34
2.6 PANalytical X'Pert PRO Materials Research Diffraction system. In orange box there are the two detectors, in the blue box there is the sample holder mounted on the goniometer, the green box includes the monochromator and automatic attenuator, in the purple box the Cu x-ray source is shown. . . 35

3.1 Setup in absorption measurements 37
3.2 Responsivity of the Ge based DET50B detector used for these measurements 39
3.3 Absorption spectra of sample 10079(HR), 10081(IR), 10082(LR). 41
3.4 Comparison of absorption spectra of samples 10039-F4, 10230-E3 and 10230-E6 42
3.5 Imaginary part of the dielectric function (ε_2) and the change ($\Delta\varepsilon_2$) induced by the presence of an electric field in a bulk semiconductor in the direct gap vicinity. 43
3.6 The generated electron-hole pair changes the occupation of the surface states 44
3.7 Setup in photoreflectance measurements 45
3.8 Photoreflectance peak example of a single transition with $A = 1$, $\varphi = \pi/2$, $E_g = 1eV$, $\Gamma = 2meV$ 46
3.9 The two signals ΔR and R measured in volt as output of the lock-in amplifier 48

4.1 XRD data of sample 10082-F6. From D the period can be defined, the 0st order peak gives information about the average concentration. 50
4.2 Simulation (purple) and data (blue) of a structure with a 12 nm Ge well and a 34 nm $Si_{0.15}Ge_{0.85}$ barrier 51
4.3 O.D. of sample 10082-F7 and the simulation considering a 14 nm pure Ge well 51
4.4 Photoreflectance spectra of sample 10082-F7 (QW) 52

4.5 Energy of the transitions HHn-cΓn as a function of n of sample 10082-F7 53
4.6 O.D. of sample 10230-E6 and the simulated absorption spectra for a 20 parabolic well 54
4.7 Photoreflectance spectrum of sample 10230-E6 with the superposed fitting 54
4.8 Absorption edge measured of sample 10039-F4 and a simulation with a well width of 70 nm 55
4.9 Comparison between the absorption spectra of a 60 nm well and a 70 nm well. Composition are the same as in 10230 56
4.10 Energy of the transitions HHn-cΓn as a function of n of sample 10230-E6 57
4.11 Energy of the transitions HHn-cΓn as a function of n of sample 10039-F4 57
4.12 Output transmission signal from the lock-in amplifiers of sample 10082 60
4.13 Output transmission signal from the lock-in amplifiers of the substrate of sample 10082 61
4.14 Output transmission signal from the lock-in amplifiers without samples 61

List of Tables

1.1 Deformation potential of Si and Ge (from reference) 26

3.1 Growth parameters of sample 10079, this procedure is defined high rate (HR). 40
3.2 Growth parameters of sample 10081, this procedure is defined intermediate rate (IR) 40
3.3 Growth parameters of sample 10082, this procedure is defined low rate (LR). 40

4.1 Comparison between calculated transitions and photoreflectance experiment 52
4.2 Comparison between the position of energy levels measured with photoreflectance and simulated (sample 10230-E6) . . . 53
4.3 Comparison between the position of energy levels measured with photoreflectance and simulated (sample 10039-F4) 55

Abstract

The goal of this master's thesis is to characterize, in terms of structural and optical properties, square and parabolic SiGe quantum-well structures.

X-ray diffraction analyses have been performed, evaluating the real size of well and barrier, and the respective Si and Ge concentrations. The absorption coefficient has been studied with transmission measurements, which allows the most important transitions to be seen. In order to better identify the transitions, experiments of photoreflectance spectroscopy have been carried out. A fitting procedure has been implemented which allows the transition energies to be found even in the difficult case of strongly overlapping transitions in the photoreflectance spectra.

A comparison between the characteristics deduced from the experiments and software simulations allows the real structure to be estimated.

Sommario

Lo scopo di questo lavoro di tesi magistrale è quello di caratterizzare, definendo proprietà strutturali e ottiche, strutture costituite da quantum-well sia quadrate che paraboliche, in SiGe.

Sui campioni è stata fatta un'analisi di diffrazione a raggi X, che permette di valutare l'ampiezza di buca e barriera, stimando anche il loro contenuto di Si e Ge. Il coefficiente di assorbimento è stato studiato con misure di trasmissione, e permette di valutare l'assorbimento da parte delle transizioni più intense. Per riuscire ad identificare meglio le transizioni, sono stati fatti degli esperimenti di spettroscopia di fotoriflessione. L'eccesiva sovrapposizione delle transizioni rende comunque difficile l'analisi dello spettro, quindi una procedura di fitting è stata resa necessaria al fine di definire in modo preciso la presenza delle diverse transizioni. Un confronto tra le caratteristiche dedotte dagli esperimenti e il risultato ottenuto da un software di simulazione consente di fare una stima sulle reali caratteristiche della struttura.

Introduction

The future innovation of data computing could be related to the photonic integration on Si based technology. The use of light in communications between microchips will allow extremely high transmission bandwidth to be reached, with low energy consumption. The required optical interconnections can be created with a Ge based multiple quantum-well growth on Si wafer, which can work as a modulator and detector.

The modulation of the signal can be performed by applying an electric field across the quantum-well structure, and thanks to the quantum-confined Stark effect the absorption coefficient can be shifted in order to absorb or not the light.

The reduced dimensionality of a quantum-well system means that the absorption coefficient depends on the properties of the structure. In a two-dimensional semiconductor system, the allowed optical transitions depend on the width and depth of the well in the conduction and valence bands.

In order to characterize these structures, different measurements are needed. X-ray diffraction experiments allow the structural properties to be defined, and optical experiments measure directly the energy of the transitions. Two types of optical measurements have been performed during this thesis work: absorption measurements, in which the absorption coefficient is defined with the detection of the light passing through the structure for each wavelength; and photoreflectance measurements, in which a modulated perturbation is applied and the change of the reflectivity is detected. Thanks to its derivative nature, photoreflectance spectroscopy allows partially superposed transitions to be resolved, which are not visible from absorption measurements.

Chapter 1

SiGe heterostructures

In this chapter I describe the importance of SiGe heterostructure nowadays for opto-electronic. These devices contain multiple quantum wells in which confined states are present. Morphologic and optical properties of these samples are described in detail in following sections. At the end of this chapter I described the software I have used to predict the positions of the quantized energy states, in order to compare the measurements with the expected values.

1.1 SiGe heterostructures in opto-electronic devices

The integration of photonic and electrical devices based on Si CMOS technology could lead the future innovation of data computing. This issue could be achieved using SiGe alloy as a waveguide and SiGe quantum wells (QWs) as modulators and photodetectors. Indeed, these devices have shown good efficiency in terms of both energy consumption and bandwidth in the telecom-

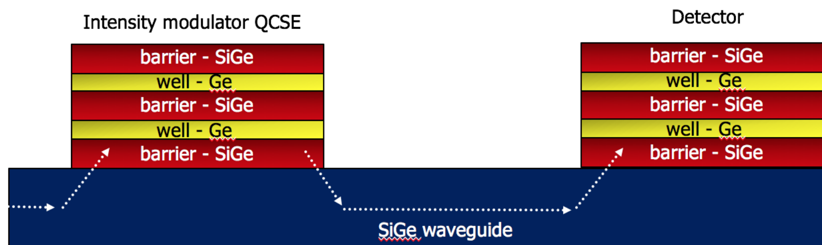

Figure 1.1: Schematic view of a modulator, waveguide and detector system

munications wavelength range[2]. In Fig. 1.1 it's possible to see how these devices work, the light coming from a laser is attracted into the modulator because of the difference in refractive index between the waveguide and QW. By applying an electric field across this structure the so-called QCSE (quantum confined Stark effect) is induced, in which electrons and holes are confined in opposite directions in the QW, and the energy difference between quantized states slightly changes. There is a red shift of the absorption coefficient. Taking advantage of this effect in the modulator we can decide whether to leave the light propagating in the waveguide or not. Once the signal reaches the photodetector it is possible to adjust the potential in order to optimize the absorption in the spectral region of the incoming light.

1.2 Square QW

One of the best known quantum mechanical problems is the infinite potential well, in which there is a confinement of a particle between two infinite potential barriers. It is possible to recreate a similar situation using two different semiconductors in which the band alignment between them reproduces well and barriers. In the real situation the barriers are finite, and this causes a small difference in the quantized energy levels of the ideal problem. Let's do some theory.

I consider the one dimensional problem, with a well of size a and the origin in the middle, so that $V = 0$ inside the well and $V = \infty$ outside. The wavefunction cannot penetrate into the barrier, so the boundary conditions impose: $\phi(a/2) = \phi(-a/2) = 0$. The solution of this problem is an infinite sequence with a quantum number $n = 1, 2, 3, \ldots$.

$$\phi_n(z) = \sqrt{\frac{2}{a}} \cos\left(\frac{n\pi z}{a}\right),\ n\,\text{odd}$$

$$\phi_n(z) = \sqrt{\frac{2}{a}} \sin\left(\frac{n\pi z}{a}\right),\ n\,\text{even}$$

We can notice that the solutions are even functions of z for odd n, and odd functions of z for even n. The energies are: $E_n = \frac{\hbar^2}{2m}\left(\frac{n\pi}{a}\right)^2$.

For the finite barrier problem the solutions are not equal to zero in the barriers. Considering for example a well a and a barrier of height V_0 with two different masses inside and outside of the well, we have to solve these two equations, the first inside and the second outside the well:

$$-\frac{\hbar^2}{2m_w}\frac{d^2}{dz^2}\phi_w(z) = E\phi_w(z)$$

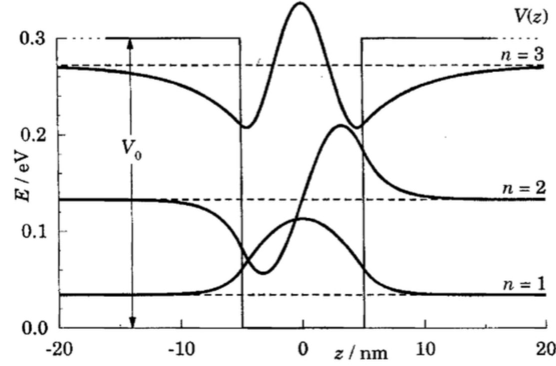

Figure 1.2: First three bound states in a GaAs finite square quantum well of width $a = 10$ nm and depth $V_0 = 0.3$ eV

$$-\frac{\hbar^2}{2m_b}\frac{d^2}{dz^2}\phi_b(z) + V_0\phi_b(z) = E\phi_b(z)$$

By applying the continuity of the wave functions at the edges and the conservation of current in the two directions we have the boundary conditions that allow this problem to be solved. As in the infinite case the solutions are alternatively symmetric and antisymmetric in z, but they are not equal to zero inside the barriers. In Fig. 1.2 are shown the first three bound states[1].

For what concerns real samples, in the bulk semiconductor the potential is periodic, and the solutions are Bloch states:

$$\psi_{\mathbf{k}}(\mathbf{r}) = u_{n,\mathbf{k}}(\mathbf{r}) \exp(i\mathbf{k} \cdot \mathbf{r})$$

where $\mathbf{k}$ and $\mathbf{r}$ are vectors. I consider the potential well as a perturbation so I can express the solutions as a linear combination of the unperturbed function, weighted using a function $\chi(\mathbf{k})$:

$$\psi_{\mathbf{k}}(\mathbf{r}) = \sum_n \left(\int_{-\infty}^{+\infty} \chi(\mathbf{k}) u_{n,\mathbf{k}} \exp(i\mathbf{k} \cdot \mathbf{r}) d^3\mathbf{k} \right)$$

We need to sum over each n because they interact with each other, but if just states with $\mathbf{k} = 0$ are considered, n can be taken equal to one for the conduction band, and two for the valence band (HH and LH), because at the Γ-point only these band are important. Another approximation could be made, since we are interested just at the center of the first Brillouin Zone (BZ), $u_{\mathbf{k}}(\mathbf{r}) = u_0(\mathbf{r})$ and we can integrate between $+\Delta\mathbf{k}$ and $-\Delta\mathbf{k}$ around

zero. The result is that the function u can be taken out of the integral, so just plane waves are weighted by the function $\chi(\mathbf{k})$:

$$\psi_k(\mathbf{r}) = u_0(\mathbf{r}) \int_{-\Delta\mathbf{k}}^{+\Delta\mathbf{k}} \chi(\mathbf{k}) \exp(i\mathbf{k} \cdot \mathbf{r}) d^3\mathbf{k}$$

where the integral is the Fourier transform of $\chi(\mathbf{k})$ and is called the Envelope function, f_{env}.
Now the problem to solve has become:

$$(H_{cryst}(\mathbf{r}) + V(\mathbf{r}))\, u_0 f_{env} = E u_0 f_{env}$$

Making the calculations the previous relation became:

$$\left(-\frac{\hbar^2\nabla^2}{2m^*} + V(\mathbf{r})\right) f_{env} = E f_{env}$$

so I can conclude that fixing the well potential and the effective mass, f_{env} can be found. So, $\psi_k(\mathbf{r}) = u_0(\mathbf{r}) f_{env}$, in which u_0 depends just on the bulk properties.

For the square potential well problem, we have to start from a three-dimensional time-independent Schrödinger equation, assuming $f_{env} = \phi(\mathbf{r})$:

$$\left[-\frac{\hbar^2}{2m}\nabla^2 + V(\mathbf{r})\right]\phi(\mathbf{r}) = E\phi(\mathbf{r})$$

Since we are dealing with a quantum well, we can simplify the problem by considering V($\mathbf{r}$) to be dependent only on the growth direction, z. In the x–y plane no potential is applied, and particles are free to move, so the wave functions are plane waves in x–y: $\phi(x, y, z) = \exp(ik_x x)\exp(ik_y y)u(z)$. We can substitute it in the last equation:

$$\left[-\frac{\hbar^2}{2m}\left(\frac{d^2}{dx^2} + \frac{d^2}{dy^2} + \frac{d^2}{dz^2}\right) + V(z)\right] e^{(ik_x x)} e^{(ik_y y)} u(z) = E e^{(ik_x x)} e^{(ik_y y)} u(z)$$

Now, the derivative in x-y and cancelling from both sides the exponential part, we get:

$$\left[-\frac{\hbar^2}{2m}\frac{d^2}{dz^2} + V(z)\right] u(z) = \left[E - \frac{\hbar^2 k_x}{2m} - \frac{\hbar^2 k_y}{2m}\right] u(z)$$

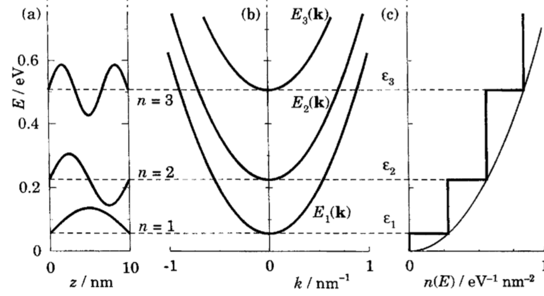

Figure 1.3: (a) Potential well with confined state placed at the right energy. (b) Total energy. (c) Density of state of a 2D system (steplike), and a 3D shape (parabolic)

Making this substitution for the energy: $E - \frac{\hbar^2 k_x}{2m} - \frac{\hbar^2 k_y}{2m} = \varepsilon$, the Schrödinger equation is: $\left[-\frac{\hbar^2}{2m}\frac{d^2}{dz^2} + V(z)\right] u(z) = \varepsilon u(z)$
So finally:

$$\phi(x, y, z) = e^{(ik_x x)} e^{(ik_y y)} u_n(z)$$

$$E_n(k_x, k_y) = \varepsilon_n + \frac{\hbar^2 k_x}{2m} + \frac{\hbar^2 k_y}{2m}$$

1.2.1 QW samples

The well potential in real samples come from the band discontinuity at the interface between different materials. In particular the conduction band offset (CBO) and the valence band offset (VBO) give rise to the confinement. Different types of band alignment can take place in heterostructure (see figure 1.4). The main difference in 1.4(a) and 1.4(c) is that for type I QWs both electrons and holes are confined in the well, instead for type II, electrons stay in the well but holes are confined into the barriers. Confining electrons in the same spatial regions has as a consequence more wavefunction overlap, and this means high absorption and recombination efficiency, which is fundamental for applications. For this reason Type I band alignments are more interesting.

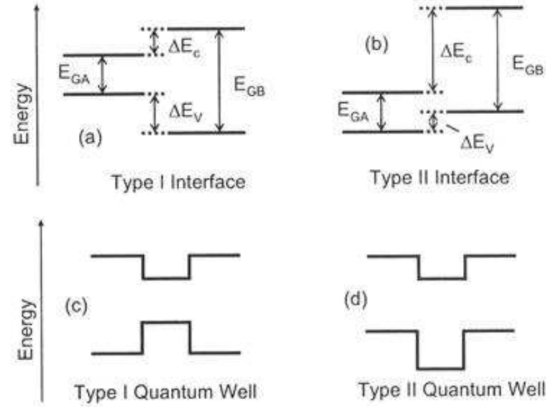

Figure 1.4: Schematic representation of Type I (a) and Type II (b) band alignment. Quantum well made of Type I (c), and quantum well made of Type II (d).

The presence of type I or II band edges depends on the heterostructure composition. Calculation of the fundamental gap, the band offset and the band alignment has been carried out by Virgilio and Grosso in Ref. [18]. The calculations are done for $Si_{1-x}Ge_x$ QWs (called active material) and $Si_{1-y}Ge_y$ barriers (called substrate) for all the possible compositions ($0 < (x, y) < 1$). The well is considered fully strained while barriers are fully relaxed. The results are shown in Fig.1.5 . VBO is positive for $x < y$ (well with less Ge content than the barriers), while is negative for $x > y$; CBO has a more complex behavior: small Ge concentration in barriers ($y < 0.3$) gives a positive CBO for almost all well content, for all the other values of x and y CBO is negative apart a small region with high Ge concentration in both well and barriers (with $y > x$). In Fig.1.5 (d), the four different situations are shown, region (iii) (high Ge content in barrier and well and $x > y$), corresponds to a type I band alignment with CBO$<$0 and VBO$>$0 and region (i) ($x < y$) corresponds to a type II with CBO$<$0 and VBO$<$0[4, 5].

All the samples studied in this thesis work have tensile $Si_{0.15}Ge_{0.85}$ barriers and pure Ge wells on a $Si_{0.1}Ge_{0.9}$ virtual substrate, so the band alignment is of type I.

The samples I studied were grown in Como at L-NESS using LEPECVD (low energy plasma enhanced chemical vapour deposition), which I explain more in detail in the next chapter. I investigated properties of sample 10082,

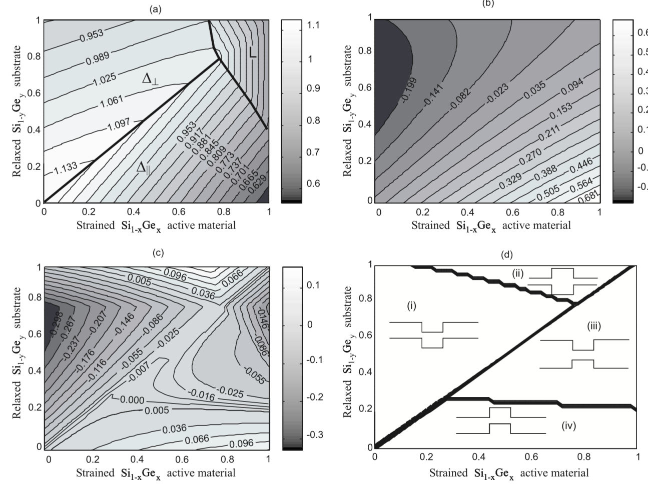

Figure 1.5: (a) Fundamental bandgap energies (with respective **k** point); (b) VBO; (c) CBO; (d) band-edge profile for QWs structure with $\mathrm{Si}_{1-x}\mathrm{Ge}_x$ layer on a $\mathrm{Si}_{1-y}\mathrm{Ge}_y$ VS.

whose structure is shown in Fig. 1.6.

As said above, in order to have type I band alignment the well has to be fully strained, while the barrier relaxed. The idea to reach this situation is to have a $\mathrm{Si}_{1-x}\mathrm{Ge}_x$ layer between silicon and QW with the right lattice parameter. This layer is called a *buffer*, and the resulting silicon substrate plus buffer becomes a *virtual substrate* (VS). In this simple VS, at the interface between the silicon substrate and the buffer the lattice parameter mismatch is too high, and the threading dislocation density reaches values of $10^8 \sim 10^9 \mathrm{cm}^{-2}$ even for low Ge content ($x \sim 0.2$)[19]. An alternative is to create a so called *graded virtual substrate* (graded VS). The buffer in this case is composed of a graded SiGe layer whose composition varies linearly from pure silicon to the desired composition. In order to reach the fully relaxed situation for the VS, a thick layer with the same composition as the final part of the graded part has to be grown, and it is called the *constant composition layer.* In a graded VS the level of threading dislocations is lowered by two or three orders of magnitude with respect to a single step VS[3, 4].

At the top of the *constant composition layer,* the QWs are grown. In sample 10082 the nominal structure is: 20 nm $\mathrm{Si}_{0.15}\mathrm{Ge}_{0.85}$ barriers and 10 nm Ge QWs; in order to increase the absorption, the QW structure is repeated 50 times. The QW thickness is non uniform across the whole wafer,

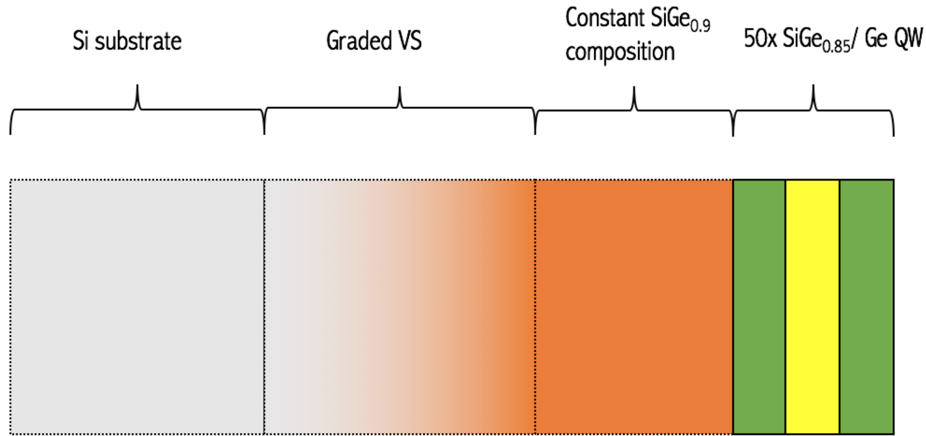

Figure 1.6: Structure of sample 10082. QW is repeated 50 times

for this reason different samples belonging to the same wafer show different structures; I will explain this feature in more detail in the next chapter.

The strain condition influences the valence band alignment in heterostructure, some considerations could be done considering the deformation potentials of silicon and germanium. If we consider a $Si_{1-x}Ge_x$ thin film grown on a $Si_{1-y}Ge_y$ substrate, it exhibits a compressive strain if $x > y$, or a tensile strain if $x < y$[4]. The presence of strained conditions causes the splitting of degenerate energy levels. Considering just the valence band at the Γ-point in reciprocal space, in the case of compressive strain the heavy hole goes up in energy, while the light hole band goes down; in case of tensile strain the opposite splitting occurs. In structure of sample 10082, the *constant composition layer* ($Si_{0.1}Ge_{0.9}$) is of course fully relaxed, and this induce a small tensile strain in the barrier ($Si_{0.15}Ge_{0.85}$), which causes a slightly splitting of heavy hole and light hole at gamma (LH goes up and HH goes down); for what concerns the well, there is a high compressive strain induced by the barrier and this causes a high energy splitting between heavy hole and light hole (HH goes up and LH goes down). The gamma, heavy hole and light hole band edges of sample 10082 are shown in Fig. 1.7.

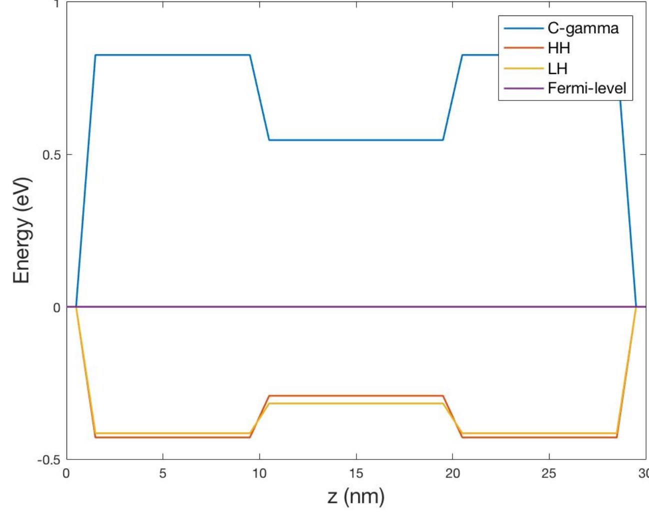

Figure 1.7: Band-edges of c-gamma, light hole and heavy hole in the growth direction of sample 10082 (10nm well and 20 nm barrier).

1.3 Parabolic QW

The problem of an infinitely deep parabolic potential well in one dimension can be related to the problem of a mass at the end of a spring:

$$V(z) = \frac{1}{2}kz^2$$

where k is the spring constant and z the displacement; the solution is an harmonic motion with a frequency $\omega_0 = \sqrt{\frac{k}{m}}$. From the quantum physics point of view we have to solve the following time-independent Schrödinger equation:

$$-\frac{\hbar^2}{2m}\frac{d^2}{dz^2}\psi(z) + \frac{1}{2}m\omega_0^2 z^2\psi(z) = E\psi(z) \tag{1.1}$$

The full derivation is quite long and I will report here just the solutions. Introducing this dimensionless variable $u = \sqrt{\frac{m\omega_0}{\hbar}}z$, the solutions are:

$$\psi_n(z) = \left(\frac{m\omega_0}{\pi\hbar}\right)^{1/4}\frac{1}{\sqrt{2^n n!}}h_n(u)\exp(-u^2/2)$$

where $n = 0, 1, 2, 3...$ is the quantum number and the functions $h_n(u)$ of order n are the Hermite polynomials. The quantized energy levels have this

form:

$$E_n = \left(n + \frac{1}{2}\right)\hbar\omega_0$$

in which is possible to notice that they are equally spaced by $\hbar\omega_0$ and with a minimum of $\frac{1}{2}\hbar\omega_0$.

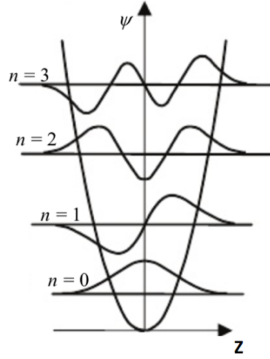

Figure 1.8: $\psi(z)$ solutions of the equation 1.1

1.3.1 PQW samples

It is possible to create a parabolic potential profile growing a crystal in which the composition vary continuously. These samples are composed by the same VS as 10082, described in section 1.2.1. For the QWs we started from $Si_{0.15}Ge_{0.85}$ and step by step, slightly changing the Ge content, we reach pure Ge in the center of the well, then course the same thing is performed in the opposite way for the other half. The process described is repeated seven times in order to increase the absorption of the parabolic structure. Since the composition of substrate and center of the QW are the same as the square case, all the considerations about the band alignment in section 1.2.1hold even in this case.

Two different growth process have been performed, in which the composition is the same but the thickness of the QW is different: sample 10039 (20 nm nominal well) and sample 10230 (40 nm nominal well), The different band edges of 10039 and 10230 are shown in Fig. 1.9. The values indicated for the well width are nominal, the real width could be slightly different, an analysis of the real thickness is done in next chapters. The consequence of a narrower or wider well is that the quantized energy levels are more or less confined at the bottom of the well.

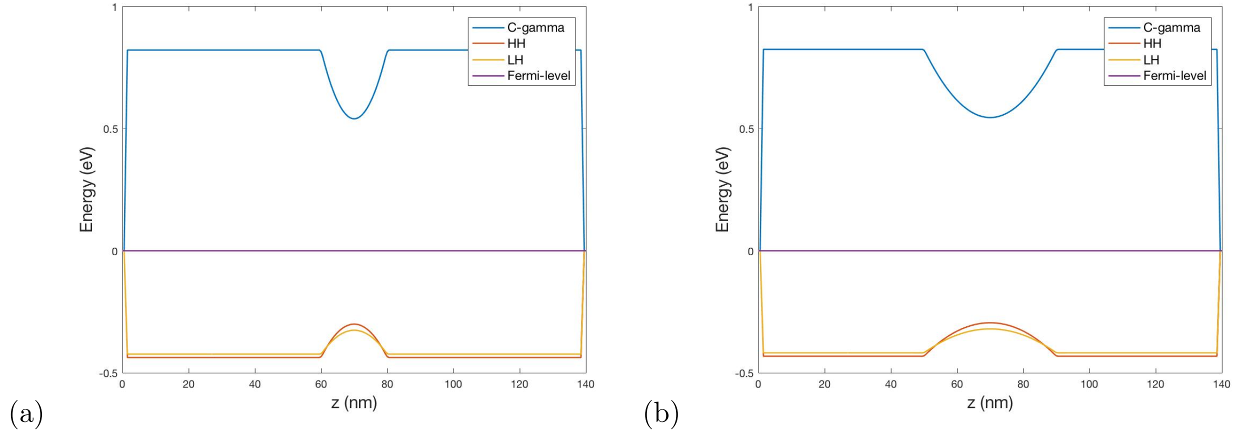

Figure 1.9: Conduction and valence band-edges at Γ point for (a)10230 nominal thickness and (b)10039 nominal thickness

The conduction band profile with the square modulus of the confined solutions calculated with *Nextnano* are shown in figure 1.10.

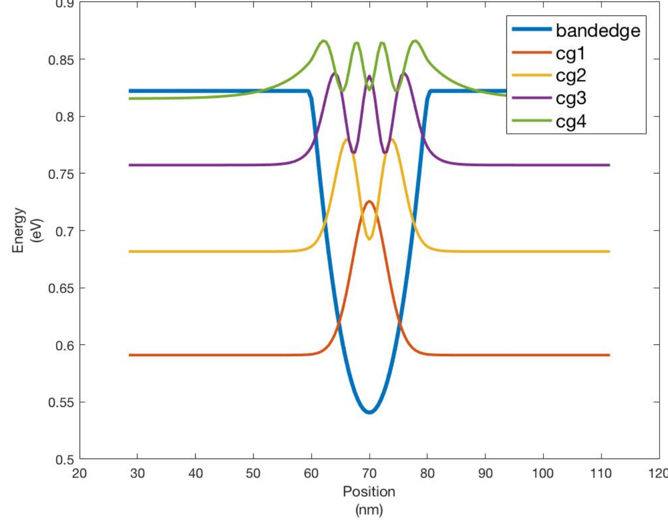

Figure 1.10: Band-edge of the conduction band at the Γ point. Square modulus of confined solutions is shown. The barrier is $SiGe_{0.85}$ while the central point of the well is pure germanium, the calculations are made using Nextnano

1.4 Optical properties of Quantum Wells

The evaluation of the absorption coefficient allows us to understand some important properties of these samples. In this section I describe how the absorption coefficient is related to the electronic states; a description in terms of the envelope function is given, allowing us to define intra-band and inter-band optical transitions. At the end I will give a brief description of excitons and how they affect the absorption spectrum.

1.4.1 Inter-band and intra-band transition

Transitions between states of the same or different bands could take place. From the Fermi Golden rule, the absorption rate is:

$$W_{if} \propto (< f \mid (\mathbf{e} \cdot \mathbf{p}) \mid i >)^2 \delta(E_f - E_i - \hbar\omega)$$

where $\mathbf{p}$ is the momentum operator and $\mathbf{e}$ is the polarization of the incoming light. In the bra-ket, $\mathbf{e}$ can be simply taken out, and the initial and final state are those calculated in the previous section, in which the envelope

function appears. Considering just the direct transition and applying the approximation that the envelope function is constant in each period of $u(z)$, we get this result:

$$< f \mid (-i\hbar\nabla) \mid i > = -i\hbar \left(\int g_i^* g_f dz \right) \left(\int_{cell} u_i^* \nabla u_f d^3\mathbf{r} \right)$$
$$\times - i\hbar \left(\int g_i^* \nabla g_f dz \right) \left(\int_{cell} u_i^* u_f d^3\mathbf{r} \right)$$

Looking at the integrals containing u, it is possible to notice that for symmetric u_i and u_f the first one goes to zero while the second not; remembering the significance of u_i and u_f, it means that the transition goes from a valence band state to another valence band state, so the second term is related to intra-band transition. In the opposite way, for antisymmetric u_i and u_f (transition between valence and conduction band), the second term is zero while the first one not, so it is related to inter-band transitions. Looking at the term containing the envelope functions in the inter-band relation, if g_i and g_f are antisymmetric it goes to zero, it means that only transition between states with the same parity are allowed. In my thesis I exploit properties of the samples in the inter-band transition range of the spectrum.

1.4.2 Absorption coefficient in 2D system

The absorption coefficient is defined as the sum of W_{if} over all the possible energy states (inter-band transitions):

$$\alpha \propto \sum_{n,m,k} (< c_m \mid (\mathbf{e} \cdot \mathbf{p}) \mid v_n >)^2 \cdot \delta(E_{c,m,k} - E_{v,n,k} - \hbar\omega)$$

where n and m indicate the particular state of valence and conduction band respectively. Making these summations it comes out that the absorption is proportional to the JDOS, the joint density of states[6]. Reminding that $DOS_{2D} = \frac{m}{\pi\hbar^2}$ (constant), the JDOS looks like a steplike function, in which the height of each step depends on the reduced mass of that particular transition.

Peaks appear in the absorption coefficient at the edge of each transition due to excitons. What happen is that when a photon is absorbed an electron is promoted to the conduction band leaving a hole in the valence band. In this description there are two particles with opposite charge placed in the same

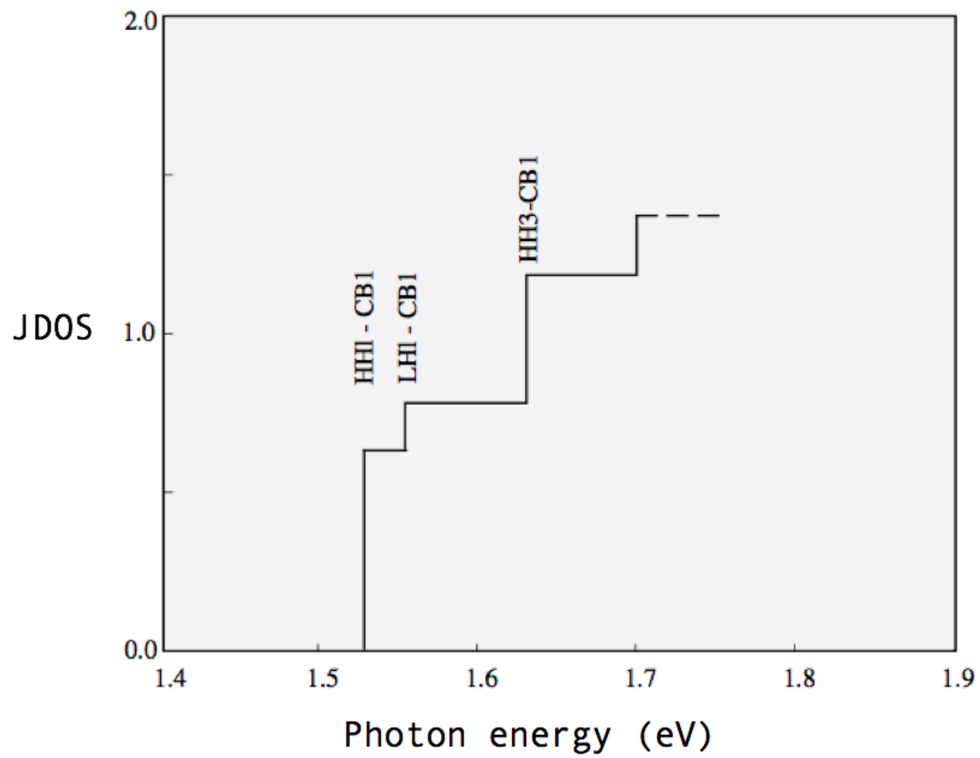

Figure 1.11: Example of a JDOS for a 2D system (from reference [6]).

spatial region, they have to be treated as a unique quasi-particle, the exciton. Solving this problem with a Coulomb interaction in the Hamiltonian, the results are the same as for hydrogen-like atoms:

$$E_n = -\frac{m_r^* e^4}{32\pi^2 \epsilon^2 \hbar^2} \frac{1}{n^2}$$

with ${m^*}_r$ the effective reduced mass which depends on the effective masses of the electron in the conduction band and of the hole in valence band[6]. Since the interaction is attractive the energy is negative, the consequence is that below each transition there is a series of quantized states. In general for samples described in section1.2.1 the maximum of E_n (E_1) is 2-10 meV. Measuring the absorption spectrum it is not possible to see any of these states because they are too close to each other, the result is that a quite large peak appears before the transitions. This effect is present even in bulk semiconductors, but since there is no confinement E_1 is almost four time smaller than in the QW case[6].

1.5 *Nextnano* Software

Nextnano is a software package which allows the behavior of nano-devices to be simulated. The use of this software has been fundamental for this thesis: the most difficult part is to assign each peak to a particular transition, and apart from the first (HH1-cΓ1), this work is not straightforward. *Nextnano* helped me to understand the order and relative intensity of the transitions.

This software make use of a database which contains the characteristics of a large number of semiconductors. Once the particular structure is defined by the user, by applying the $\mathbf{k} \cdot \mathbf{p}$ method the band-structure is calculated. The $\mathbf{k} \cdot \mathbf{p}$ method is applied by the software considering for the conduction band just the Γ point, and for the valence the heavy hole, light hole bands; this means that only direct absorption is calculated.

The deformation potential utilized in the simulation are reported in Table 1.1, according with reference [20]. The parameters a_v , b and $d$are the deformation potential of the valence band, the first is related to the hydrostatic deformation, while second and third to uniaxial; a_c^Γ, a_c^L, a_c^X , Ξ_u^Γ, Ξ_u^L and Ξ_u^Δ are the hydrostatic and uniaxial deformation potential of the conduction band at different points in the reciprocal space.

The calculated absorption spectra do not contain the exciton effect. The *Nextnano* calculated wavefunction solutions are imported into a *Matlab* program, and for each transition a solution of the excitonic problem is found by

Parameter	Silicon	Germanium
a_v (eV)	1.80	1.24
b (eV)	−2.10	−2.86
d (eV)	−4.85	−5.28
a_c^{Γ} (eV)	−10.39	−10.41
a_c^{L} (eV)	−0.66	−1.54
a_c^{X} (eV)	3.3	2.55
Ξ_u^{Γ}	0.0	0.0
Ξ_u^{L}	16.14	16.2
Ξ_u^{Δ}	8.6	9.42

Table 1.1: Deformation potential of Si and Ge (from reference)

applying the variational method. Since we have a two-particle problem, we look for solution of the form $\phi(\rho) \propto e^{-\rho/\lambda}$, which is of the same form as the 1s orbital solution (λ is the parameter to find). Minimizing the functional:

$$E[\psi] = < \psi \mid H \mid \psi >$$

the approximated solution of the problem is found. The Hamiltonian depends on the particular transition we are considering and contains three terms: the kinetic energy and the Coulomb interaction between the two. The kinetic term depends on the effective mass of electron (in the conduction band) and hole (in the valence band); the effective mass for electrons in the conduction band is unique, while the effective mass of holes depends of the particular starting state of the transition (heavy hole or light hole). The interaction term is created starting from the eigenfunction of the initial and final state generated by the simulation, in particular it depends on the overlap integral of the two states; intuitively if the overlap is high it means that the two particles are confined in the same position inside the well, and the Coulomb interaction is high. Once the functional is minimized, from the solution it is possible to define the Bohr radius ($\lambda = a_0$), and the energy is defined as the exciton energy, which is negative because of the attractive Coulomb interaction. In order to compare the measured absorption spectrum with the simulated spectrum, we have to perform these calculations for each transition and then reconstruct the total absorption considering this effect.

Chapter 2

Sample growth and XRD analysis

In this chapter I briefly describe the low-energy plasma-enhanced chemical vapor deposition technique. In order to analyze the structural properties of the samples an x-ray diffraction study is performed which allows us to define the real composition and thickness of the heterostructures.

2.1 LEPECVD

Low-energy plasma-enhanced chemical vapor deposition is used for the epitaxial growth of high quality Si and SiGe heterostructures. This technique is capable of growing epitaxial material with exceptionally high rates at substrate temperatures below 600°C[14].

In standard CVD processes the precursors gases (silane SiH_4 and germane GeH_4, for Si and Ge) are thermally decomposed on the substrate. In UHV-CVD (ultra-high vacuum chemical vapour deposition) excellent crystal quality has been demonstrated but the growth rate at low substrate temperature (below 600°C) become exceedingly low[13, 14, 15]. In order to lower the substrate temperature while maintaining a high rate of growth a plasma can be used in the so-called *plasma enhanced* CVD, in which the precursor activation energy is provide by a plasma. However the high ion energies in radio frequency plasmas can cause damage at the surface. To solve this problem a low-energy plasma-enhanced CVD has been implemented.

The LEPECVD technique involves the use of a low-voltage direct current arc discharge to sustain the plasma, which maintains the plasma ions at low energy (10 eV)[4]. A schematic representation of the LEPECVD deposition

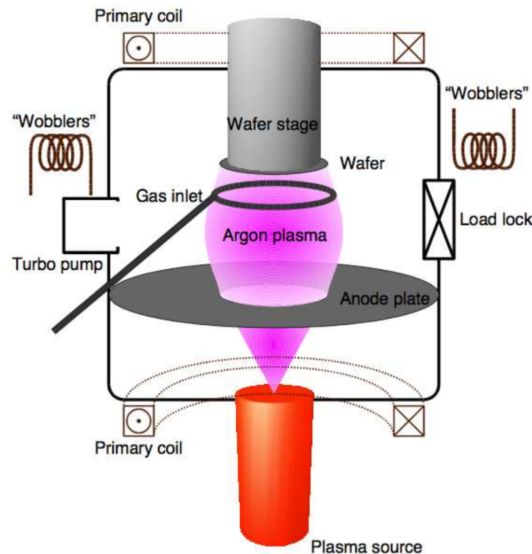

Figure 2.1: Schematic representation of the LEPECVD deposition chamber

chamber is shown in Fig. 2.1. The plasma source consists of a tantalum filament which is current heated to the point of thermoionic emission. Argon gas is passed through the source into the chamber, and a high-intensity direct current arc is struck between the source and the chamber; an anode ring is mounted within the growth chamber to stabilize the discharge. In order to control the plasma density and position, a magnetic field generated with two coils (above and below the chamber) is used.

Many parameters affect the sample growth, such as substrate temperature, precursor gas flux, or plasma intensity. For samples studied in this thesis work the temperature during the growth process is kept constant at around 500°C. In general three different growth rates are used depending on the gas flux and the plasma intensity; they are defined as LR (low rate), IR (intermediate) and HR (high rate). In section 3.1.3 these different methods are described in detail and a comparison between optical measurements of the three is shown.

The plasma density and the injection of the gases into the chamber is non-uniform, the consequence is that the real thickness of the deposited material onto the wafer is also non-uniform. In figure 2.2 is shown a map of the wafer indicating the ratio between the deposited thickness and the nominal thickness. For this reason the position on the wafer of each measured sample

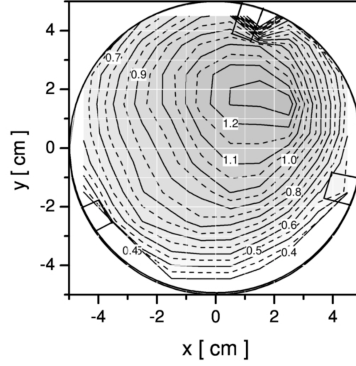

Figure 2.2: Ratio between thickness of deposited material and nominal

has to be known.

2.2 XRD analysis

In this thesis work high resolution x-ray diffraction measurements are performed with the use of a PANalytical X'Pert PRO diffractometer. In this section a general introduction of the theory behind kinematical diffraction is given and the particular data obtained from a QW structure are described with Fourier transform considerations. At the end the diffractometer system is defined in detail.

2.2.1 Von Laue condition

This explanation is founded on the kinematic theory, in which three approximations take place: for the incident radiation the scattering from the atoms is assumed to be elastic (the modulus of $\mathbf{k}$ is constant), the scattered waves are spherical and phenomena such as absorption, reflection and interference are neglected. The diffracted wave field is assumed to be weak.

The mathematical treatment of the Laue condition is now described starting from the situation in figure 2.3. The amplitude of the x-rays at point P is given by:

$$A_P = A_0 e^{i\mathbf{k}_0 \cdot (\mathbf{R}+\mathbf{r}) - i\omega_0 t}$$

where A_0 is the amplitude, $\mathbf{k}_0$ the wave vector and ω_0 the angular frequency, the vector $\mathbf{R}$ is the distance between the source and a scattering center which is taken as the origin, $\mathbf{r}$ is the vector describing the distance between

the origin and the scattering centers, in this case P. Since each atom is a scattering center, the light reaching the detector (placed at point B) is the sum of all the spherical waves generated at each scattering point. The total amplitude can be expressed as:

$$A_B = A_P(\mathbf{r}, t)\varrho(\mathbf{r})\frac{e^{i\mathbf{k}\cdot|\mathbf{R}'-\mathbf{r}|}}{|\ \mathbf{R}' - \mathbf{r}\ |}$$

where $\varrho(\mathbf{r})$ is defined as the complex scattering density which takes into account the amplitude and the phase of the scattered plane waves, $\mathbf{R}'$ is defined as the position of the detector with respect to the origin and $\mathbf{k}$ is the wave vector of the scattered wave. As said above, since the scattering event is elastic ω_0 does not change, and the factor $\varrho(\mathbf{r})$ is time-independent because the material is rigid. The total amplitude reaching the detector is defined as the integration of the previous formula over the total investigated region, where A_P is substituted. The total intensity is then:

$$I(\mathbf{K}) \propto |\ A_B\ |^2 \propto \left| \int \varrho(\mathbf{r}) e^{-i\mathbf{K}\cdot\mathbf{r}} d\mathbf{r} \right|^2$$

with $\mathbf{K} = \mathbf{k} - \mathbf{k}_0$. Since the complex scattering density is a periodic function, it can be expressed as its Fourier transform:

$$\varrho(\mathbf{r}) = \sum_{\mathbf{G}} \varrho_{\mathbf{G}} e^{i\mathbf{G}\cdot\mathbf{r}}$$

where $\mathbf{G} = h\mathbf{g}_1 + k\mathbf{g}_2 + l\mathbf{g}_3$ is a generic vector of the reciprocal lattice with $\mathbf{g}_1, \mathbf{g}_2, \mathbf{g}_3$ the three unit vectors of reciprocal space and h,k,l are integers. Substituting this Fourier transform into the intensity:

$$I(\mathbf{K}) \propto \left| \int \sum_{\mathbf{G}} \varrho_{\mathbf{G}} e^{i\mathbf{G}\cdot\mathbf{r}} e^{-i\mathbf{K}\cdot\mathbf{r}} d\mathbf{r} \right|^2 \propto \left| \sum_{\mathbf{G}} \varrho_{\mathbf{G}} \int e^{i(\mathbf{G}-\mathbf{K})\cdot\mathbf{r}} d\mathbf{r} \right|^2$$

in which the main contribution from the integral is given when $\mathbf{G} = \mathbf{K}$. This is the Laue condition: if the difference between the initial and final wave vector ($\mathbf{k}_0$ and $\mathbf{k}$) is a vector belonging to the reciprocal lattice, then there is a diffraction peak.

An important consequence of the Laue condition can be defined starting from the incident light with wave vector $\mathbf{k}$: in order to have diffraction there has to exist a vector $\mathbf{G}$ of the reciprocal lattice such that the projection of $\mathbf{k}$ on $\mathbf{G}$ is equal to half the modulus of $\mathbf{G}$. This fact can be demonstrated easily with geometrical considerations. As said above $\mathbf{G} = \mathbf{K} = \mathbf{k}_0 - \mathbf{k}$,

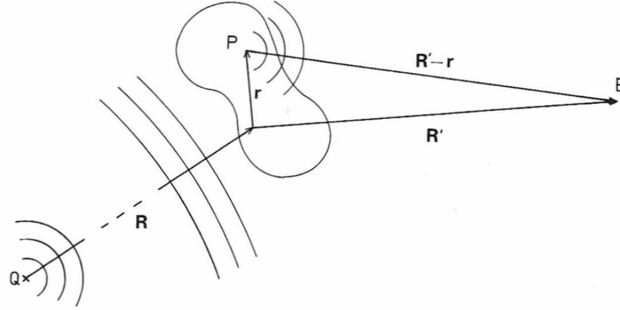

Figure 2.3: Schematic representation of x-ray scattering in a lattice. Q, B, P are respectively the source, the detector and a generic scattering center. The vector **r** relate the origin of the system and the scattering point P.

inverting this equation it is possible to write $\mathbf{k} = \mathbf{k}_0 - \mathbf{G}$, since the modulus of these two vectors has to be the same:

$$| \mathbf{k} |^2 = (\mathbf{k}_0 - \mathbf{G}) \cdot (\mathbf{k}_0 - \mathbf{G}) = | \mathbf{k}_0 |^2 + | \mathbf{G} |^2 - 2 | \mathbf{k}_0 | \cdot | \mathbf{G} |$$

but we are considering just elastic scattering events, so the modulus of the initial and final wave vector are equal. Moreover expressing $\mathbf{G}$ as a versor ($\mathbf{n}_G$) multiplied by the modulus ($| \mathbf{G} |$) the resulting relation is:

$$\mathbf{k}_0 \cdot \mathbf{n}_G = \frac{1}{2} | \mathbf{G} |$$

this means that the projection of $\mathbf{k}_0$ on the direction of $\mathbf{G}$ has to be equal to $| \mathbf{G} | /2$.

2.2.2 $\omega - 2\theta$ Scan in a QW structure

The main objective of this study is to understand the real width of the quantum well, so we are interested in the characteristic of the sample only in the growth direction. A large angle coplanar geometry has been used, this means that the incident and scattered vector lie in the same plane which is orthogonal to the surface of the sample. The surface of the sample is a (0 0 1) plane and the sample is aligned making the incident and the scattered vectors lie in the (1 1 0) plane. This configuration allows us to detect diffraction peaks (h k l) in which h=k. Because of the symmetry of SiGe crystal, only peaks in which h, k and l are all odd, or h, k and l are all even, with h+k+l

equal to a multiple of 4, are allowed. Since we are interested in understanding the structural properties in the growth direction, only the (0 0 4) diffraction peak has been considered, which give information about $q_{\perp}$.

In the $\omega-2\vartheta$ scan the incident (ω) and diffracted ($2\theta/2$) angles are almost the same and this provide properties of symmetric diffraction peaks (0 0 l). In this type of scan the length of $\mathbf{q}$ is varied while the direction remains constant. The x-axis can be changed from $\theta(^{\circ})$ to $q_{\perp}(1/nm)$ by the relation:

$$q_{\perp} = \frac{2}{\lambda}\sin(\theta)$$

Remembering that the kinematical diffraction is essentially the Fourier transform of the real-space lattice, some considerations can be made. I consider a quantum well structure with a well width d and a barrier width b, the total width is $d + b = D$. First of all the situation of a well defined rectangular profile containing the atoms in the real lattice can be seen as a multiplication between a series of delta function (atoms) and a rectangle (width d), thinking in term of reciprocal space it is a convolution between a series of a delta functions and a *sinc* function. This means that the intensity of a particular diffraction peak is a $sinc^2$ instead of a delta, and the distance between two zeros is proportional to the inverse of the width of the rectangle ($1/d$). Moreover the presence of well repeated n times, as in the MQW samples, can be seen as a convolution between a series of deltas (separated by D) and a rectangle (width nD) which in reciprocal space become a multiplication between another series of deltas with a *sinc*. The last consideration could be done even for the barrier with the same conclusions, of course since it is wider than the well the *sinc* is narrower. At the end the result is to have a diffraction spectra in which a set of narrow peaks with spacing proportional to $1/D$ is modulated by two $sinc^2$ (one with width proportional to $1/d$ and the other proportional to $1/b$). An intensity spectra of sample 10082 is shown in figure 2.4 with the superimposed $sinc^2$, note that the plot is logarithmic. The position of the two sinc functions will depend on the composition of well and barrier, the position of the zero order peak shown in figure define the average lattice constant which allows us to find the average SiGe content of the structure.

2.2.3 'Xrayutilites' simulation

For what said above, average content and total period can be found easily by looking at the position of the peaks, while the thickness of well and barrier separately is more difficult to find because the effect of the two modulating

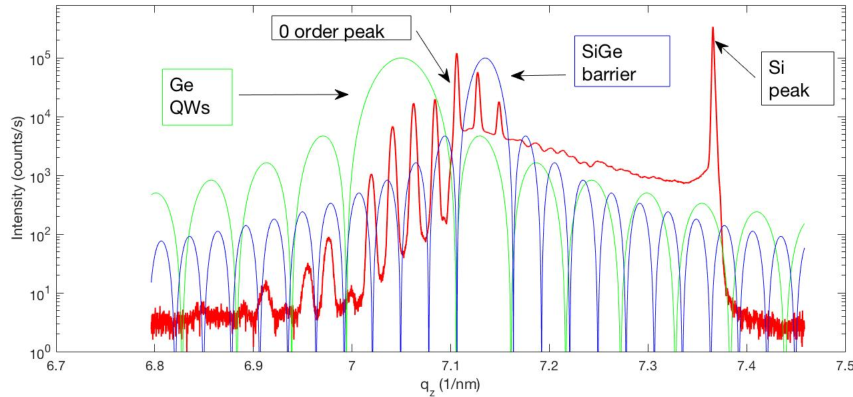

Figure 2.4: $\omega - 2\vartheta$ scan of the (0 0 4) peak of sample 10082-F7, in red the measured intensity is shown, the green curve is due to the Ge wells while the blue one is due to the SiGe barriers.

$sinc^2$ have a less defined effect on the spectrum. For this reason we take advantage of simulations in order to estimate real thicknesses and compositions. The simulation procedure is done with *xrayutilies*, which is a Python package that allows us to analyze and simulate x-ray diffraction data.

Defining all the characteristic of the structure *xrayutilities* simulates a $\omega - 2\theta$ scan which is compared with the data. In the simulation well and barrier thickness and compositions have to be chosen following the conditions of average composition and total period which are known from the spectrum.

For what concerns the parabolic quantum well samples, an XRD $\omega - 2\theta$ scan is shown in figure. The parabolic shape of the well makes the simulations more difficult to perform and the definition of real thickness and composition cannot be done precisely.

2.2.4 XRD diffractometer

For SiGe film characterization we have used a PANalytical X'Pert PRO Materials Research Diffraction system, which is shown in Figure 2.6. This is a high resolution diffractometer that allows us to deduce valuable data of the films grown. Data include all types of information regarding the lattice structure of the analyzed materials, such as the lattice parameters, composition, thickness, and then strain level and plastic relaxation of layer. The x-ray tube uses a copper anode, and a two-bounce Ge(220) hybrid monochromator and mirror is used to select the Cu Kα_1 line at a wavelength of $\lambda = 0.15406$

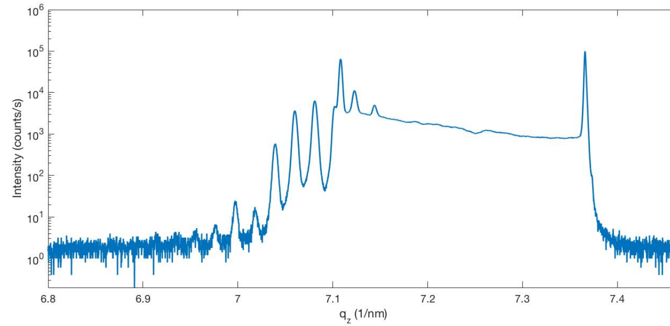

Figure 2.5: XRD $\omega - 2\vartheta$ around the (0 0 4) diffraction peak of a PQW sample

nm. The intensity of the direct beam is $> 10^8$ counts/s. An automatic attenuator is activated in order to prevent damage to the detectors in the case of intense diffraction peaks. Thanks to the goniometer on which the sample holder is mounted, it is possible to control: x, y and z position of the wafer with 1–10 μm precision; the angle ω between incident beam and the specimen surface and the scattering angle 2ϑ with 0.0001° precision, and the tilt angle χ and the azimuthal angle φ in 0.01° steps. This system features two Xe proportional detectors, one of them is used for alignment (it has a large 1° aperture) of the samples and the other for high resolution measurement due to the presence of a Ge analyzer crystal.

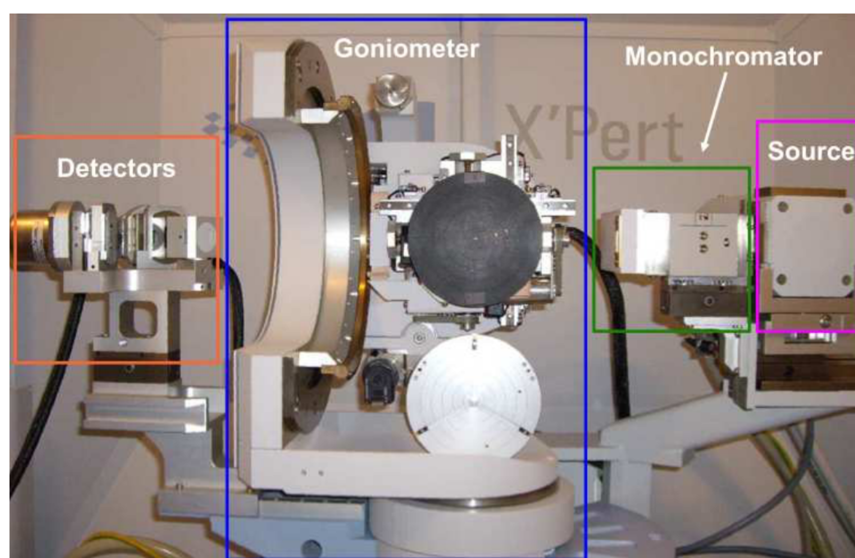

Figure 2.6: PANalytical X'Pert PRO Materials Research Diffraction system. In orange box there are the two detectors, in the blue box there is the sample holder mounted on the goniometer, the green box includes the monochromator and automatic attenuator, in the purple box the Cu x-ray source is shown.

Chapter 3

Absorption and photoreflectance measurements

As explained in section 1.4.2, in the absorption spectrum the position of the transitions depends of the composition and width of the well and the height of the barriers. From the comparison between XRD analysis and absorption spectrum, composition and thickness of the heterostructure con be defined. Instead, the definition of the band-alignment in SiGe heterostructure is particularly difficult not just because of the large lattice mismatch but also because the conduction-band minima in Si and Ge are located at different points away from the BZ center [17]. In reference [16] they have calculated the natural band offsets between semiconductor compounds, using an all-electron band structure approach taking into account the deformation potential of the core states. Following these calculations we fixed a VBO (valence band-offset) equal to 0.8 eV in the simulation program *Nextnano*.

In this chapter I explain the instrumental setup and the theory behind both absorption and photoreflectance measurements. Then the resulting spectra for QW and PQW structure are shown.

3.1 Absorption measurements

The definition of the absorption coefficient in case of two dimensional system has been described in section 1.4. The measurement consists of the detection of the transmitted light from the sample for a particular wavelength selected with a monochromator. A scan over a wide region is performed, usually from 1100 to 1600 nm and the light signal is converted to current with a detector and amplified as described in following section. It could be better

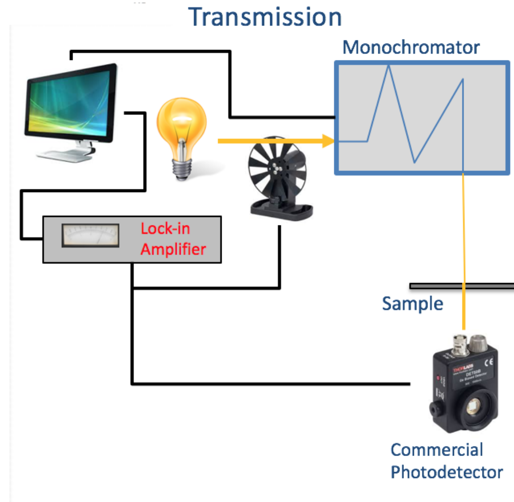

Figure 3.1: Setup in absorption measurements

to analyze even at high photon energy in order to exploit absorption of high energy states, but because of the presence of the indirect absorption edge of silicon (1.11 eV at room temperature) no light can pass throughout the thick silicon substrate. The indirect gap for germanium at room temperature is 0.66 eV and this means that it contributes to the absorption, but since pure Ge is present only inside the well (a few nanometers), the effect of indirect absorption in these measurements is negligible.

In order to obtain the absorption signal from the QWs we have to subtract the component absorbed by the VS, which is measured directly in another sample with the same composition of the VS. Of course the alignment of the samples in these two measurements is not perfectly equal, and an adjusting factor has to be taken into account, as described in Appendix A.

3.1.1 Setup in absorption measurement

In absorption measurements the light coming from a halogen lamp passes through a monochromator, is focused on the sample, and then reaches the detector. In order to increase the signal to noise ratio a lock-in amplifier is used; the modulation is imposed using a chopper, placed between lamp and monochromator.

The halogen lamp has a spectral emission which is quite constant in the region of interest. The light beam is modulated by a chopper with the modulation frequency set at 400 Hz. The monochromator is directed by a

computer through a LabVIEW panel, which allows a scan to be run over a certain spectral region with fixed steps of $\Delta\lambda_1 = 1$ nm. The bandpass of the monochromator is $\Delta\lambda_2(\text{nm}) = lineardisp\left(\frac{\text{nm}}{\text{mm}}\right) \cdot aperture(\text{mm})$, where linear dispersion is an internal characteristic (12.9 nm/mm) and the aperture is the outgoing window $(10 - 70\,\mu\text{m})$, in all cases $\Delta\lambda_1 > \Delta\lambda_2$ so there is no superposition between two different steps. Before the sample two gold mirrors and a series of lenses are placed in order to focalize the beam on the sample.

For the detection a Ge based DET50B is used, which guarantees a good responsivity between 800 and 1700 nm (see figure 3.2). The current signal from the detector is than converted to a voltage signal, using a transimpedance amplifier with adjustable gain $(10 - 10^6)$. In order to enlarge the signal to noise ratio a double-phase lock-in amplifier (LBH090-PAR5206) is used, whose inputs are the amplified signal coming from the detector and the reference signal from the chopper. The principle behind a lock-in amplifier is that on multiplying two general AC signals the results are two different components, one at a frequency equal to the sum of the two, and the other at a frequency equal to the difference. In this setup, since reference and signal have the same frequency, the multiplication between reference and optical signal is DC, while the noise coming from the detector is shifted by the reference frequency. At the end a low-pass filter rejects every noise component. In the lock-in amplifier used in these measurements the time constant of the filter can be set to different values; in transmission experiments one second is sufficient.

3.1.2 Optical density and data acquisition

From the Lambert-Beer law:

$$I(z) = I_0 e^{-\alpha z}$$

the intensity decreases exponentially in a medium with the absorption coefficient α. In a QW the situation is different, since there is a quasi two-dimensional system: the z-dimension is no longer well-defined, and the absorption coefficient loses its meaning. This problem is overcome by the definition of optical density, or absorbance:

$$\text{O.D.}(\lambda) = -\log_{10}(I_{TS}(\lambda)/I_{TR}(\lambda))$$

where I_{TS} is the transmitted intensity of the sample (QWs and VS) and I_{TR} is the transmitted intensity from a reference (the VS). If the optical path in the two measurement slightly changes, the last formula would give wrong

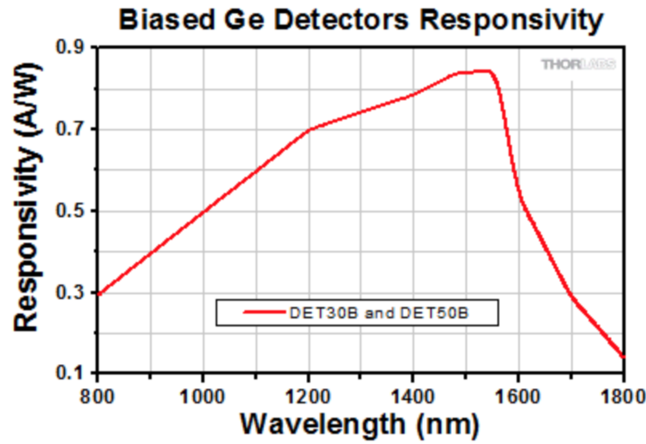

Figure 3.2: Responsivity of the Ge based DET50B detector used for these measurements

results, in Appendix A the calculations necessary to define O.D. properly are shown.

The backside of each sample presents very high roughness, and this causes scattering effects on the outgoing beam, for this reason it has to be polished before transmission measurements. This procedure is carried out using a rotative cleaner which makes the silicon backside smooth and reflective. During this process the QW-side of the sample needs to be preserved with a protective coating, which is then removed with acetone and isopropanol.

3.1.3 QW/PQW absorption measurements

As described in the introduction of the chapter, the absorption spectrum along with *Nextnano* simulations and XRD studies allows the properties of the samples to be understood. The most important information given by these spectra are the position of the quantized energy levels and the exciton peaks. In the first part of this section I show how the growth parameters affect the samples, then I describe the relation between absorption measurements and simulations with *Nextnano*. In the second part the same absorption spectra of parabolic quantum wells have been measured.

In Fig. 3.3the absorption spectra of samples 10079, 10081, 10082 are shown. These three samples are nominally the same, but they are grown with different growth procedures, see tables 3.1, 3.2, 3.3. All these samples are composed of:

- Virtual Substrate: thick Si with a graded buffer (graded from Si to $Si_{0.10}Ge_{0.90}$)
- Quantum well: 10 nm QW (Ge) and 20 nm barrier ($Si_{0.15}Ge_{0.85}$)

Time (s)	Si flux (%)	Ge flux (%)	I_{Arc} [A]	I_{Coil} [A]
3	11.00	80.00	50	9
1	11.00	80.00	50	9

Table 3.1: Growth parameters of sample 10079, this procedure is defined high rate (HR).

Time (s)	Si flux (%)	Ge flux (%)	I_{Arc} [A]	I_{Coil} [A]
13	17.50	80.00	30	3
8	17.50	80.00	30	3

Table 3.2: Growth parameters of sample 10081, this procedure is defined intermediate rate (IR)

Time (s)	Si flux (%)	Ge flux (%)	I_{Arc} [A]	I_{Coil} [A]
53	3.00	17.00	30	3
28	3.00	20.00	30	3

Table 3.3: Growth parameters of sample 10082, this procedure is defined low rate (LR).

These samples differs from in terms of growth rate. The growth rate depends on three parameters: the process gas flux into the chamber, the arc discharge current I_{Arc}, and the coil confinement current I_{Coil}; the latter two parameters determine a difference in the plasma density. The maximum gas flux is 25 sccm (Standard Cubic Centimeters per Minute), in Tables 3.1, 3.2 and 3.3 the percentage of this maximum value is reported. In the LR growth case (sample 10082) both the plasma density and the flux are set to low values, in fact it takes a long time. For what concerns the IR growth (sample 10081) the plasma density is still low, while the flux is high. The HR growth is characterized by high values of the plasma density and the flux. In Fig. 3.3 the three spectra are different from each other: the samples have different quantized energy levels. The first thing to notice is that on increasing the growth rate, the absorption shifts to higher energy. There are two possible

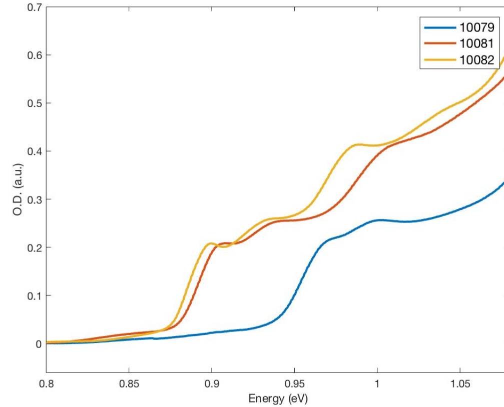

Figure 3.3: Absorption spectra of sample 10079(HR), 10081(IR), 10082(LR).

motivation behind this fact: the quantum well is shorter, and this causes the increasing of the first quantized energy state, or the well is note composed by pure Ge (the band-gap of $Si_{1-x}Ge_x$ is greater than Ge gap for each value of x). Other information can be obtained by looking at the exciton peaks. In a well-defined structure, with sharp band edges, the electrons and holes are more confined in the QW and the exciton effect is more visible.

With parabolic well samples these measurements are more complicated because the energy levels are closer together and therefore difficult to resolve. In any case some dissimilarity between absorption coefficients of different samples can be noted. I have studied three different samples:

- 10039 F4
- 10230 E3
- 10230 E6

All these samples have the same composition, $Si_{0.15}Ge_{0.85}$ barriers and a well composition that goes from $Si_{0.15}Ge_{0.85}$ to pure Ge in the central point. In Fig. 3.4 the absorption spectra of the three samples is shown. The different width of the well, as explained in the first chapter, determines the position of the energy states, in fact for larger wells, the states are closer togethr at the bottom of the well, with the result is that the energy gap is smaller. In figure 3.4 the absorption edge shift is clear, larger the well, smaller the gap. Another consequence of larger well is that the quantized energy levels are close to each other. In fact from section 1.3, the spacing between energy level

is $\Delta E_n = \hbar\omega_0$, where $\omega_0 \propto \sqrt{k}$, since the energy difference between the two extrema of the well is the same (the height of the well does not change), for larger well k is smaller and as a consequence ΔE_n is lower. In figure 3.4this is well visible, in 10039-F4 spectrum no quantized levels are resolved, just a smooth increasing absorption is present. Instead, in the sample 10230-E6 two small steps are visible at 0.94 eV and 1.02 eV, which are more defined in sample 10230-E3 at 0.96 and 1.05 respectively. The first step of both the sample is of course related to the first, and more intense, transition which is the HH1-cΓ1 , for the second one is more difficult to associate with a transition, it could be LH1-cΓ1 or HH2-cΓ2.

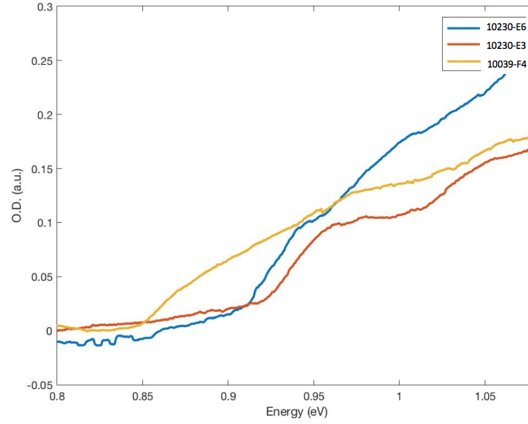

Figure 3.4: Comparison of absorption spectra of samples 10039-F4, 10230-E3 and 10230-E6

3.2 Modulation spectroscopy

Modulation spectroscopy is a technique which, taking advantage of a modulated perturbation, allows us to measure the derivative, with respect to the energy, of the dielectric function. Different types of modulation spectroscopy experiments could be done; in this thesis I have performed photoreflectance, which has the same characteristics of the electroreflectance.

The dielectric function contains information about the joint density of states, which takes the form of broad bands with some superimposed Van Hove singularities[7] corresponding to the optical transitions. But these transitions cannot be resolved by measuring the dielectric function directly. With electroreflectance a change in the dielectric function is imposed, and this

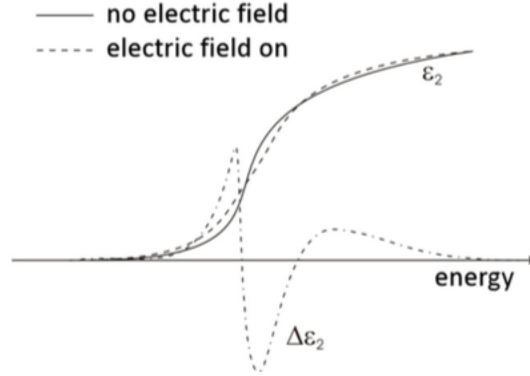

Figure 3.5: Imaginary part of the dielectric function (ε_2) and the change ($\Delta\varepsilon_2$) induced by the presence of an electric field in a bulk semiconductor in the direct gap vicinity.

spectral change is more evident in correspondence of the Van Hove singularities. Since the reflectivity depends of the dielectric function, the changes induced by the electric field can be resolved.

The electroreflectance consists of a measurement of the differential reflectivity of a sample, on which a modulated electric field is applied. Defining the Seraphin coefficients (α, β) the relative change in reflectivity can be expressed as:

$$\frac{\Delta R}{R} = \frac{R - R'}{R} = \alpha(\varepsilon_i, \varepsilon_r)\Delta\varepsilon_r + \beta(\varepsilon_i, \varepsilon_r)\Delta\varepsilon_i$$

Where R and R' are the reflectivity coefficients when the field is on and off respectively, and α and β depend on the unperturbed dielectric function[8]. The effect of the presence of an electric field on ε is more pronounced in correspondence of optical transition, in figure 3.5 the electro-induced change in the imaginary part of the dielectric function for a bulk semiconductor close to the direct gap is shown. It has been demonstrated that in the case of bulk semiconductors, the quantity $\Delta\varepsilon$ is proportional to the third derivative of ε [9] . However for bound states such as in a quantum well, the electric field cannot accelerate the electron in the growth direction, so they behave as particles with infinite mass in that direction. These particles do not have translational symmetry because they are confined in space and this causes $\Delta\varepsilon$ to be proportional to the first derivative of ε[10]. The change of the

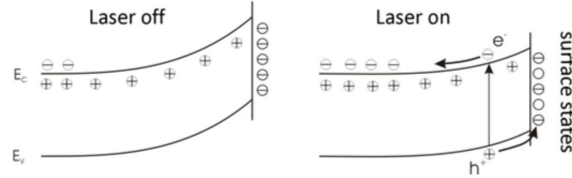

Figure 3.6: The generated electron-hole pair changes the occupation of the surface states

dielectric function can be approximated as:

$$\Delta\varepsilon = \left[\frac{\partial \varepsilon}{\partial E_g} \frac{\partial E_g}{\partial F_{a.c.}} + \frac{\partial \varepsilon}{\partial \Gamma} \frac{\partial \Gamma}{\partial F_{a.c.}} + \frac{\partial \varepsilon}{\partial I} \frac{\partial I}{\partial F_{a.c.}} \right] F_{a.c.}$$

where E_g is the energy gap, $F_{a.c.}$ is the modulated electric field, I is the integrated intensity, and Γ is the broadening parameter[11](see reference [9] for more detail). The form of $\Delta\varepsilon$ depends on the shape of the unperturbed dielectric function, which could be either Gaussian or Lorentzian, depending on the broadening mechanism or temperature.

Photoreflectance is a non-invasive type of electroreflectance in which the electric field is induced in the growth direction with the use of a light beam. The advantage of using photoreflectance instead of electroreflectance is its contactless nature, so that no preparation of the sample, such as the fabrication of contacts, is needed. In this technique the modulating light is generated by a laser and the photon energy has to be higher than the band gap, in order to be absorbed. When the light reaches the semiconductor electrons and holes are generated which are free to move and cause a change in the occupation of the surface states (fig. 3.6). This motion creates a difference in the curvature of the band at the surface which can be seen as an electric field.

3.2.1 Setup in photoreflectance measurements

The setup is almost the same as in the absorption measurements, apart from the presence of the laser and various measures which have to be taken to decrease the noise. In photoreflectance experiments the reflected light from the sample is measured, so the detector has to be placed at the correct angle. Since the signal is very low an alignment optimization of the beam has to be performed. The chopper is placed in front of the perturbing beam, which

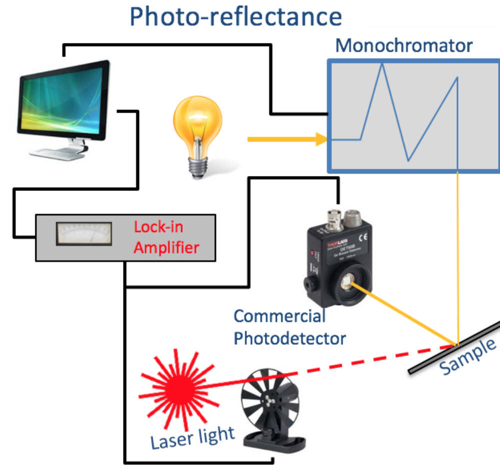

Figure 3.7: Setup in photoreflectance measurements

comes from a HL6358MG laser with an emission wavelength of 639 nm. The emission power of the laser can be set to different values (0-10 mW), with a power of 9 mW being sufficient for these measurements. Since the signal is very low (few μV at the lock-in amplifier), the integration time of the lock-in needs to be set to least at three seconds and the noise level is still high. In order to increase the signal to noise ratio, for each wavelength the output value is the mean of different values of the signal.

3.2.2 Data acquisition and fitting

In order to understand the position and the amplitude of the energy transitions a least square fitting between data and a reference formula is performed. In the case of uniform broadening, it is possible to express the relative change in the reflectivity coefficient for a single transition as:

$$\frac{\Delta R}{R} = Re\left\{Ae^{i\varphi}(E - E_g + i\mathit{\Gamma})^{-n}\right\}$$

where A is the amplitude of the signal, φ is the phase with respect to the modulating factor, E_g is the energy gap and Γ is the broadening parameter [12]. The parameter n depends on the form of the unperturbed dielectric function; for a Lorentzian shape it has to be set to $n = 2$ and the function is defined as the FDLL (first derivative Lorentzian line-shape), instead for a Gaussian shape $n = 3$ and it is called the FDGL (first derivative Gaussian

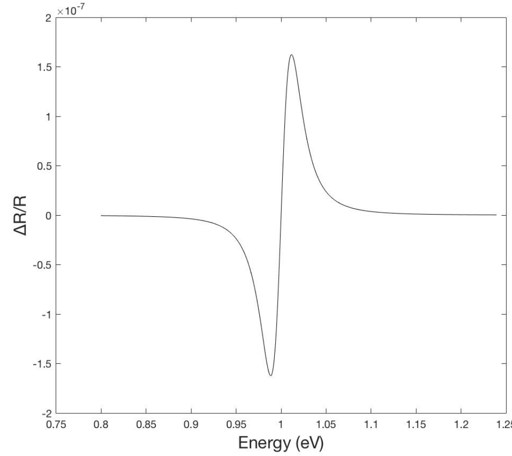

Figure 3.8: Photoreflectance peak example of a single transition with $A = 1$, $\varphi = \pi/2$, $E_g = 1eV$, $\Gamma = 2meV$

line-shape). For bound states such as quantum well structures, the FDLL is more appropriate [12].

According to this function, two measurements need to be performed: ΔR and R. For the first, the setup is exactly as described is section 3.2.1, instead for the second the laser is turned off and the chopper is placed between the lamp and the monochromator. The two measurements depend on many non-ideal parameters, for example the non-constant spectral emission from the lamp and the non-uniform responsivity of the detector, but in any case the division between ΔR and R make these effects vanish, the only consequence being that when the two signals are small the noise contribution becomes slightly more important.

The fitting procedure is performed with a Matlab script, which is a least squares fitting between the measured $\frac{\Delta R}{R}$ and the right-hand side of the FDLL, defined as the test function. For each transition four parameters are fitted: A, φ, E_g, Γ. Each of these values has a meaning in the position and shape of the photoreflectance peak. A is the amplitude of the Lorentzian, φ is a symmetry parameter (if $\varphi = \pi/2$ the shape is perfectly symmetrical), E_g is the transition energy and Γ determines how sharp the peak is. A typical shape of a photoreflectance peak is shown in figure 3.8.

3.2.3 Measurements

Spectra of quantum well samples feature a lot of transitions close to each other; the photoreflectance peaks are superimposed and the identification of each transition is not straightforward. For this reason the test function has to contain all the transition at the same time, and it is not possible to fit each transition independently from the others which complicates the fitting process. Usually the least squares fit needs to be run many times before good results are obtained. Two different approaches are possible: trying to fit a wide part of the spectrum with a great number of transitions in the test function or gradually fitting a small part of the spectrum with a few transitions and then at the end reconstructing the total spectrum. A compromise between these two is the best method, sometimes the presence of a superposition of just two photoreflectance peaks is clear and in this case the second approach is preferable, in other cases the number of superposed structures is higher and the first method is more convenient.

In figure 3.9the output signals from the lock-in amplifier of ΔR and R of sample 10082-F7 are shown, above 1.3 eV the amplitude of the transitions decreases and recognizing different structures become impossible. Anyway below 1.3 eV there is a well defined signal containing a lot of peaks.

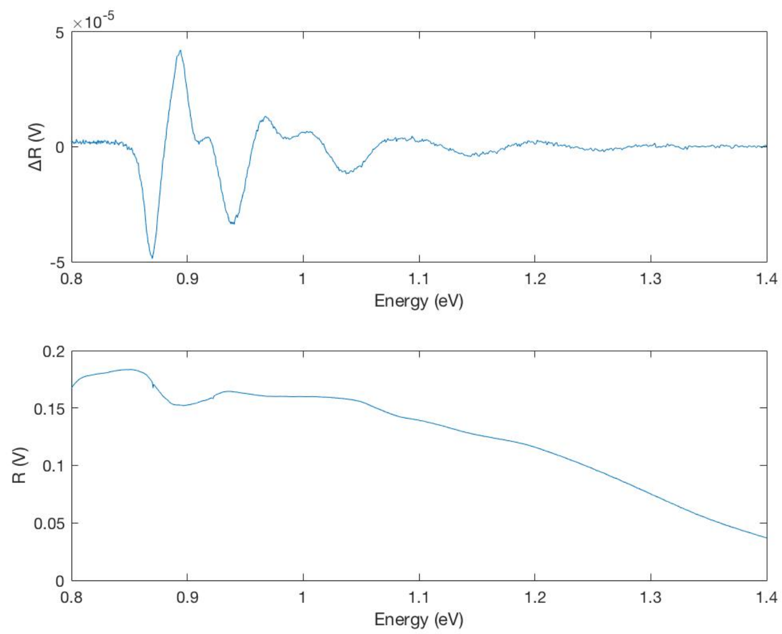

Figure 3.9: The two signals ΔR and R measured in volt as output of the lock-in amplifier

Chapter 4

Results

In this chapter the three different types of measurements described in this thesis are compared (XRD, absorption, and photoreflectance), which allow the samples to be characterized from three different points of view.

In the case of square QWs a complete characterization can be carried out, since all the parameters are available. From analysis of the XRD spectrum the thickness and composition of the wells and barriers can be estimated. Starting from the XRD values, structures with similar compositions and thicknesses have been simulated. Comparing measured and simulated absorption spectra allows the best-fitting structure to be identified. A final comparison with the photoreflectance measurement has been done, which allows first to compare simulation and data at higher energy and second to resolve the precise position of the quantized energy states inside the well.

For what concerns the PQW samples, the analysis is more difficult because the XRD spectra do not give a direct estimation of the thicknesses. Anyway, the thickness of the well can be estimated from the absorption spectra, even if it is not well defined as in the previous case. Moreover, by analyzing the photoreflectance spectra, a comparison between higher energy states can be carried out. Two different samples of this type have been characterized, 10230-E6 (20 nm nominal well) and 10039-F4 (40 nm nominal well).

4.1 Square QW

Absorption and photoreflectance measurements were performed on sample 10082-F7, while XRD measurement and simulation were performed on sample 10082-F6, of course the composition of the two is the same because they

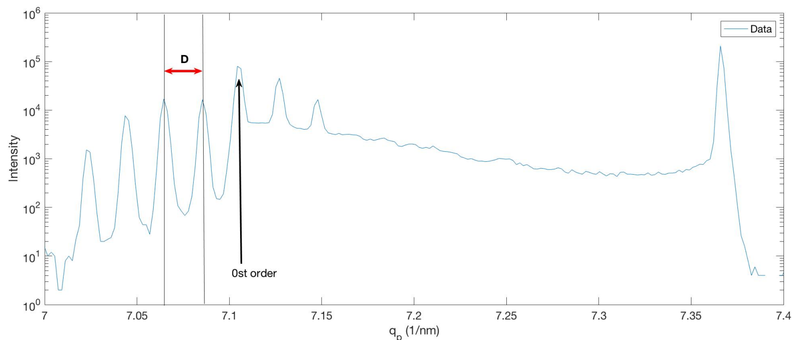

Figure 4.1: XRD data of sample 10082-F6. From D the period can be defined, the 0st order peak gives information about the average concentration.

are parts of the same wafer, instead the thickness of wells and barriers can slightly change between the two. From the thickness map shown in figure 2.2, we can infer that the wells in sample F6 are a little bit thinner than in sample F7. The XRD spectrum of sample 10082-F6 is shown in figure 4.1. The period of the structure is equal to the inverse of D and the average Ge content determines the position of the 0th order peak. From the figure, the period is estimated around 46 nm, and the average content of $Si_{1-x}Ge_x$ with x equal to 0.89. The simulated spectrum is shown in figure 4.2. The simulation fits almost perfectly, this allows us to estimate the well to be pure germanium, with a width of 12 nm, while the barrier is composed by $Si_{0.15}Ge_{0.85}$ and a width of 34 nm.

In order to simulate the change in Ge content between barrier and well, in the simulation an intermixing region is created, in which the Ge content changes continuously between 0.85 to 1. The intermixing zone is done using an *error function*, with this shape of the well the less confined levels see a larger well, and the consequence is that their energies are slightly lower than in a perfect square situation.

The comparison between measured and simulated absorption spectra, allows the width of the well of sample 10082-F7 to be inferred to be around 14 nm. In Figure 4.3 a plot of the two curves is shown.

The photoreflectance signal is fitted with the procedure described in Section 3.2.2, in which the number of the transitions utilized in the procedure is chosen looking at the contribution to the absorption given by each of them. The resulting fitting is shown in Fig. 4.4, the two curves coincides along all the spectrum, in Table 4.1, the expected values of transition energies (from the simulation) and the values extrapolate from the fitting are

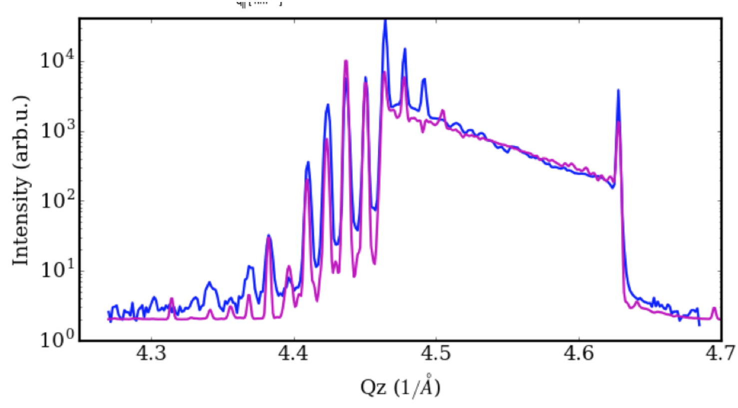

Figure 4.2: Simulation (purple) and data (blue) of a structure with a 12 nm Ge well and a 34 nm $Si_{0.15}Ge_{0.85}$ barrier

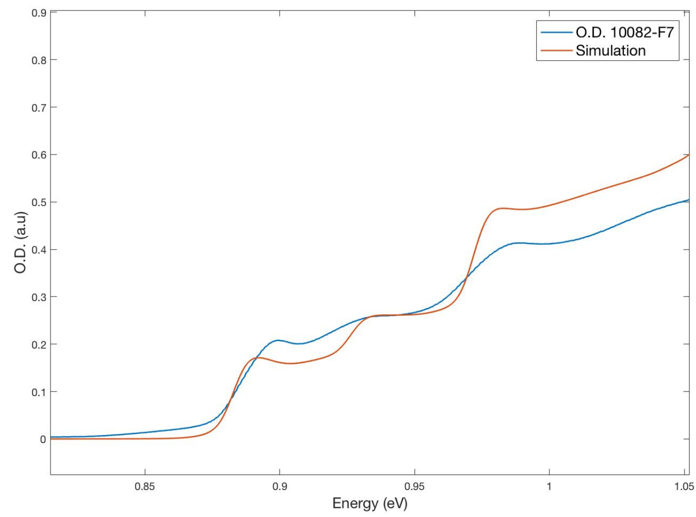

Figure 4.3: O.D. of sample 10082-F7 and the simulation considering a 14 nm pure Ge well

Transition	HH1-cΓ1	HH2-cΓ1	LH1-cΓ1	HH3-cΓ1	HH2-cΓ2	HH3-cΓ2	HH3-cΓ3
Experiment [eV]	0.87	0.896	0.912	0.937	0.979	1.037	1.154
Calculated [eV]	0.871	0.899	0.912	0.93	0.986	1.025	1.128

Table 4.1: Comparison between calculated transitions and photoreflectance experiment

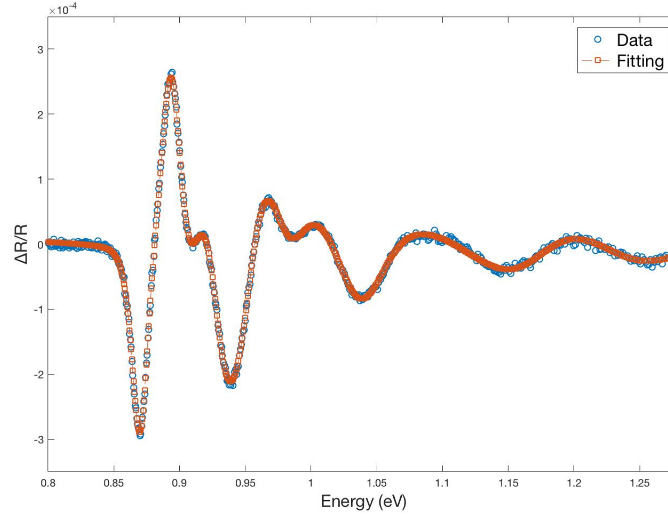

Figure 4.4: Photoreflectance spectra of sample 10082-F7 (QW)

compared. The good correspondence between simulations and experiments allows to confirm that the structure defined in the simulations corresponds to the sample.

As defined in the first chapter, the energy separation between transitions of type HHn-cΓn, in the case of square wells, is proportional to n^2. Since there are two valence bands (heavy hole and light hole) we have two different series. For what concerns the light hole series, we have just one transition, instead in the heavy hole series we have three transitions. In Figure 4.5 , the energy of the transitions are plotted as a function of n, and while three points are not many to compare a parabolic shape can be inferred.

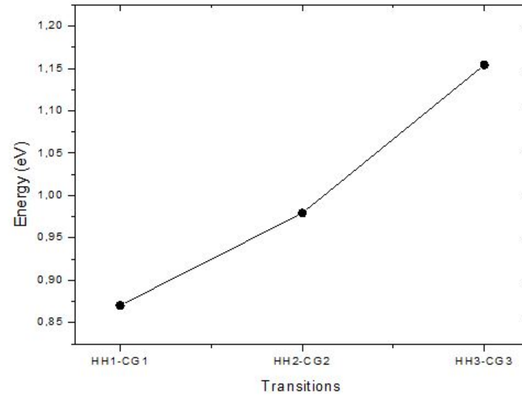

Figure 4.5: Energy of the transitions HHn-cΓn as a function of n of sample 10082-F7

Transition	HH1-cΓ1	HH2-cΓ1	HH3-cΓ1	HH2-cΓ2	HH1-cΓ3	HH3-cΓ3
Experiment [eV]	0.91	0.94	0.977	1.029	1.078	1.143
Calculated [eV]	0.903	0.939	0.967	1.026	1.07	1.133

Table 4.2: Comparison between the position of energy levels measured with photoreflectance and simulated (sample 10230-E6)

4.2 Parabolic QW

XRD spectrum in case of parabolic wells is not so easy to interpret, while the estimation of the thickness can be inferred looking at the edge of the absorption and at the photoreflectance spectrum.

The position of the first quantized level in the valence and conduction bands determines the energy gap. For larger well the levels are closer to the bottom of the well and the consequence is to see a smaller energy gap in the absorption spectra.

Sample 10230-E6 has a nominal thickness of 20 nm. Comparing the absorption spectrum and the position of the transitions obtained with photoreflectance measurements, the well is estimated to be 20 nm. The comparison of the edge of the absorption spectra are shown in Fig. 4.6, and the fitted photoreflectance curves in Fig. 4.7. The position of the obtained transitions (see Table 4.2) is in complete agreement with the expected ones, this allows us to believe that the width of the well is to a good approximation 20 nm.

In sample 10039-F4 the experimental absorption profile does not exhibit the 2-dimensional steplike shape because of the vicinity of the energy levels,

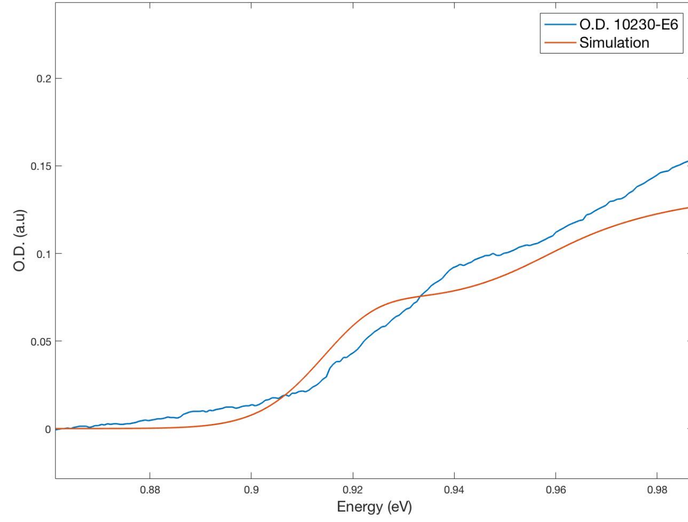

Figure 4.6: O.D. of sample 10230-E6 and the simulated absorption spectra for a 20 parabolic well

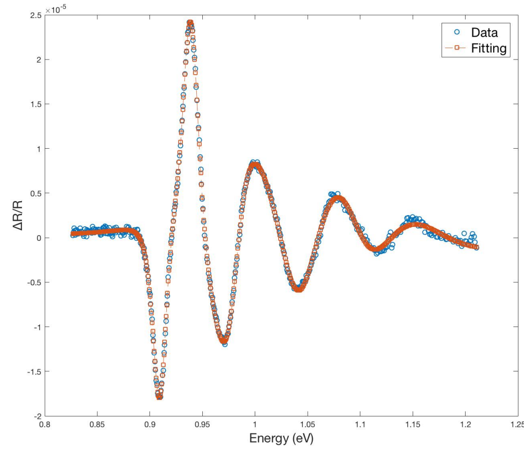

Figure 4.7: Photoreflectance spectrum of sample 10230-E6 with the superposed fitting

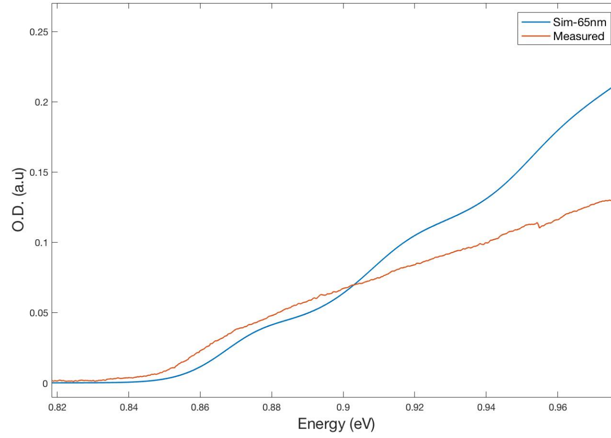

Figure 4.8: Absorption edge measured of sample 10039-F4 and a simulation with a well width of 70 nm

Transition	HH1-cΓ1	HH3-cΓ1	HH2-cΓ2	HH4-cΓ2	HH3-cΓ3	HH4-cΓ4
Experiment [eV]	0.855	0.883	0.902	0.927	0.958	0.979
Calculated [eV]	0.869	0.887	0.9083	0.927	0.946	0.983

Table 4.3: Comparison between the position of energy levels measured with photoreflectance and simulated (sample 10039-F4)

and the comparison between different simulations becomes more difficult. The nominal width of the well is 40 nm, but comparing the measurements of absorption and photoreflectance the estimation of the well width is 70 nm. The correspondent absorption spectrum is shown in Fig. 4.8.

In this kind of sample with a wide well, the photoreflectance spectra assume more importance with respect to other cases. In fact in the situation of a narrow well, from the absorption measurements the size of the well can be inferred more precisely. In a wide well instead, differences in the width of the well change the absorption spectra only slightly, because the first quantized levels are almost at the bottom of the well and a change in the size of the well do not affect its energy. In figure 4.9the spectra of two samples with the same composition as 10039 is shown, the optical gap is the same in the case of a 60 nm well and a 70 nm well. The position of the transitions obtained from photoreflectance are compared with the simulations in Table 4.3. Apart from the first transition which differs by 13 meV, all the other

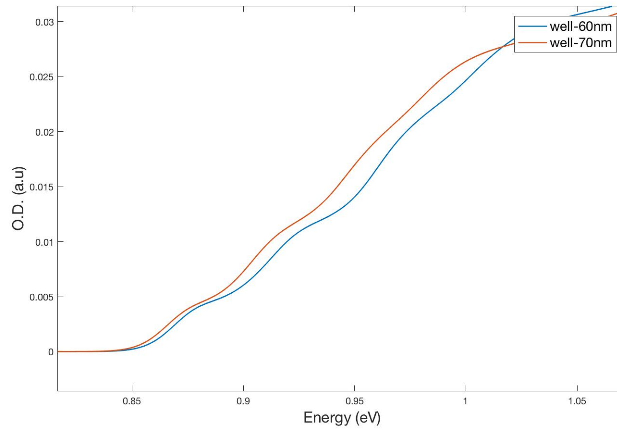

Figure 4.9: Comparison between the absorption spectra of a 60 nm well and a 70 nm well. Composition are the same as in 10230

values are very closed to the simulated ones.

The plot of the transitions with the same quantum number is shown in Figure 4.10 and in Figure 4.11; in sample 10230-E6 three transitions of this type are detected, while in sample 10039-F4 we have four of them. The last transition of sample 10039-F4 appears to be lower than the expected value, but looking at Table 4.3, it is possible to notice that the value is very close to the simulation. This happens because the well is finite and this causes less confinement for higher states and the consequence is a decreasing energy difference between adjacent states.

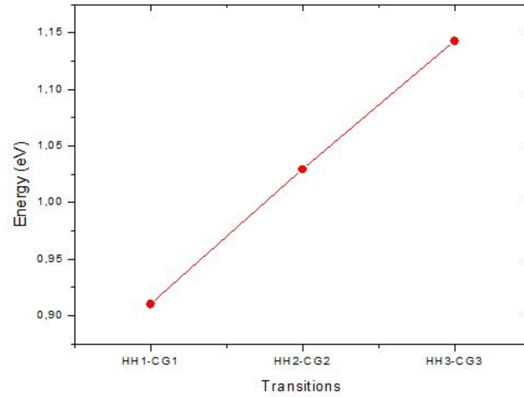

Figure 4.10: Energy of the transitions HHn-cΓn as a function of n of sample 10230-E6

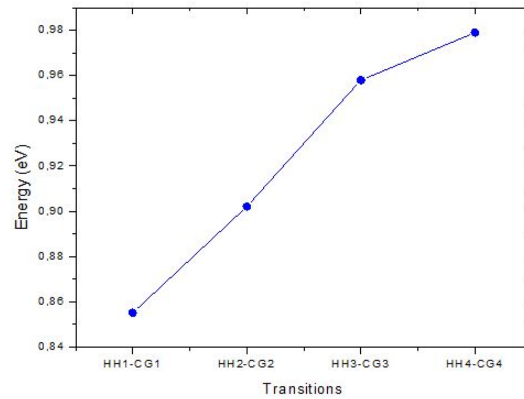

Figure 4.11: Energy of the transitions HHn-cΓn as a function of n of sample 10039-F4

Conclusions

In conclusion, the three methods together allow quantum well samples to be properly characterized, defining in a clear manner all the characteristics of the particular sample.

In case of square quantum well, XRD and absorption measurements would be enough to understand thickness and composition of the well, anyway photoreflectance spectroscopy gives the exact position of the more intense transitions even at high energy, which in our case allows us to give an estimation of the width of the intermixing zone.

For what concern the parabolic well, it is hard to get information with both XRD and absorption measurements, in this case photoreflectance spectroscopy is the only method which allows us to demonstrate the parabolic shape of the well.

In order to go further in the characterization process a possibility is to perform photoreflectance at low temperature, which could have the effect of making the shape of each transition narrower. The consequence would be a more defined structure with reduced superposition, which would allow transitions at higher energy to be identified. In this case the plot of the series of transitions shown in the last chapter, would give more evidence of the shape of the well.

Appendix A-Transmission measurements

To define the optical density of a QW-sample three measurements are necessary:

- $I_1(\lambda)$, transmission of quantum well grown on the VS
- $I_2(\lambda)$, transmission of the VS
- $I_0(\lambda)$, the signal without any sample

The first two signal are defined as:

$$I_1(\lambda) = I_0(\lambda) \exp(A_{QW}(\lambda) + c_1 A_S)$$

$$I_2(\lambda) = I_0(\lambda) \exp(c_2 A_S)$$

where A_{QW} and A_s are the absorbance of quantum well and substrate respectively. By taking the logarithm:

$$\ln\left(\frac{I_1(\lambda)}{I_0(\lambda)}\right) = A_{QW}(\lambda) + c_1 A_S$$

$$\ln\left(\frac{I_2(\lambda)}{I_0(\lambda)}\right) = c_2 A_S$$

because of the differences of optical path of measurements and polishing of samples, $c_1 \neq c_2$, and A_{QW} is not just the difference between the two previous expression. Dividing the second expression by c_2 , and substituting in the first one:

$$\ln\left(\frac{I_1(\lambda)}{I_0(\lambda)}\right) = A_{QW}(\lambda) + \ln\left(\frac{I_2(\lambda)}{I_0(\lambda)}\right)\frac{c_1}{c_2}$$

But noting that at small energy ($\lambda > 1600$␣nm) the quantum well does not absorb anymore it is possible to approximate $A_{QW}(\lambda > 1600\,\mathrm{nm}) \simeq 0$:

$$\ln\left(\frac{I_1(\lambda > 1600)}{I_0(\lambda > 1600)}\right) \simeq c_1 A_S$$

and dividing all this expression by $\ln(I_2/I_0)$:

$$\frac{c_1}{c_2} = \frac{\ln\left(\frac{I_1(\lambda>1600)}{I_0(\lambda>1600)}\right)}{\ln\left(\frac{I_2(\lambda)}{I_0(\lambda)}\right)}$$

so that at the end, substituting in the first expression:

$$A_{QW}(\lambda) = \ln\left(\frac{I_1(\lambda)}{I_0(\lambda)}\right) - \frac{c_1}{c_2}\ln\left(\frac{I_2(\lambda)}{I_0(\lambda)}\right)$$

In this derivation I've used ln instead of $\log_{10}$ as defined in chapter 3, which is only a multiplication by a constant value.

In figure the measurements of I_0, I_1 , I_2 of sample 10082 (see section 1.2.1) are shown.

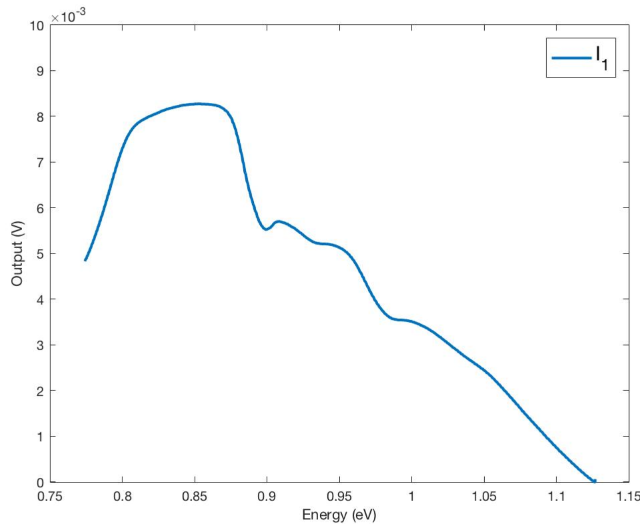

Figure 4.12: Output transmission signal from the lock-in amplifiers of sample 10082

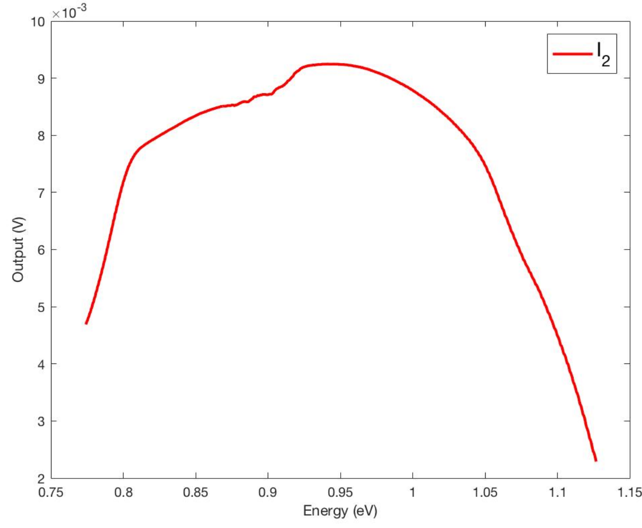

Figure 4.13: Output transmission signal from the lock-in amplifiers of the substrate of sample 10082

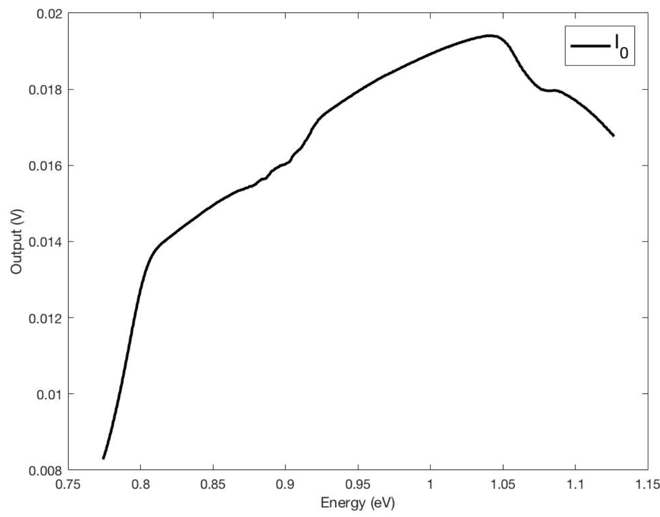

Figure 4.14: Output transmission signal from the lock-in amplifiers without samples

Bibliography

[1] Davies, John H. *The physics of low-dimensional semiconductor: an introduction.* Cambridge, Cambridge University (1998)

[2] Papichaya Chaisakul, Delphine Marris-Morini, Jacopo Frigerio, Daniel Chrastina, Mohamed-Said Rouifed, Stefano Cecchi, Paul Crozat, Giovanni Isella, Laurent Vivien. Nat. Photonics 8, 482–488 (2014)

[3] E. A. Fitzgerald et al. Applied Physics Letters, 59-811 (1991)

[4] Bonfanti Matteo, *Ge multiple quantum wells: electronic states and optical properties* (2008)

[5] M. L. W. Thewalt, D. A. Harrison, C. F. Reinhart, and J. A. Wolk. *Type II Band Alignment in Si12xGex Si 001 Quantum Wells: The Ubiquitous Type I Luminescence Results from Band Bending.* Physical Review Letters, 79-269 (1997)

[6] Jasprit Singh. *Electronic and Optoelectronic Properties of Semiconductor Structures.* Cambridge, Cambridge University (2003)

[7] Peter Y. Yu, Manuel Cardona. Fundamentals of Semiconductors: Physics and material properties. Stuttgart, Springer

[8] B. Seraphin, N. Botta. Physical Review, 145-628 (1966)

[9] Fred H. Pollak, H. Shen. Material science and engineering 10, 7-8 (1993)

[10] W. S. Chi, Y. S. Huang. Semiconductor Science and Technology 10, 127-137 (1995)

[11] D.Y. Lin, Y. S. Huang, K. K. Tiong. Chinese journal of physics 35, 3 (1997)

[12] H. P. Hsu, P. H. Wu, Y. S. Huang, D. Chrastina, G. Isella et al. Applied Physics Letters 100, 041905 (2012)

[13] Von Känel, M. Kummer, A. Dommann, and E. Müller. Applied Physics Letters 76, 427 (2000)

[14] C. Rosenblad, T. Graf, J. Stangl, Y. Zhuang, G. Bauer, J. Schulze, H. von Känel. Thin Solid Film 336, 89-91 (1998)

[15] B. S. Meyerson. Applied Physics Letters 48, 797 (1986)

[16] Yong-Hua Li, Aron Walsh, Shiyou Chen, Wan-Jian Yin, Ji-Hui Yang, Jingbo Li, Juarez L. F. Da Silva, X. G. Gong, Su-Huai Wei. Applied Physics Letters 94, 212109 (2009)

[17] James T. Teherani, Winston Chern, Dimitri A. Antoniadis, Judy L. Hoyt. Physical Review B 85, 205308 (2012)

[18] M. Virgilio and G. Grosso. Journal of Physics: Condensed Matter, 18, 1021 (2006)

[19] F. K. LeGoues, K. Eberl, S. S. Iyer. Applied Physics Letters 60, 2862 (1992)

[20] D. J. Paul. Journal of Applied Physics 120, 043103 (2016)